https://doi.org/10.5194/egusphere-2026-2340
Preprint. Discussion started: 2 June 2026

Constraining the Vertical Profiles of Aerosol Component and Heating Rate over East Asia through Assimilating CALIOP observations

Yueming Cheng[1], Tie Dai[2], Daisuke Goto[3], Keiya Yumimoto[4], Tomoaki Nishizawa[3], Rei Kudo[5], Min Zhao[6], Akiko Higurashi[3], Yoshitaka Jin[3], Atsushi Shimizu[3], Haoran Peng[2], Guangyu Shi[2], and Teruyuki Nakajima[7]

[1] Laboratory of Atmospheric and Oceanic Dynamics, Institute of Atmospheric Physics, Chinese Academy of Sciences, Beijing, China
[2] State Key Laboratory of Earth System Numerical Modeling and Application, Institute of Atmospheric Physics, Chinese Academy of Sciences, Beijing, China
[3] National Institute for Environmental Studies, Tsukuba, Japan
[4] Research Institute for Applied Mechanics, Kyushu University, Fukuoka, Japan
[5] Meteorological Research Institute, Japan Meteorological Agency, Tsukuba, Japan
[6] State Key Laboratory of Tibetan Plateau Earth System, Environment and Resources, Institute of Tibetan Plateau Research, Chinese Academy of Sciences, Beijing, China
[7] Atmosphere and Ocean Research Institute, The University of Tokyo, Kashiwa, Japan

Correspondence to: Tie Dai (daitie@mail.iap.ac.cn) and Yueming Cheng (chengyueming@mail.iap.ac.cn)

Abstract. The vertical distribution of distinct aerosol components fundamentally governs atmospheric shortwave heating rates and radiative effects. However, traditional data assimilation (DA) methods typically rely on total aerosol optical thickness (AOT) or extinction, which fails to constrain the specific aerosol composition and often leads to the misallocation of aerosol between scattering and absorbing species. To address this limitation, we develop a component-resolved four-dimensional local ensemble transform Kalman filter (4D-LETKF) system with spatial and observational constraints within the WRF-Chem model. This novel system assimilates CALIOP-MODIS synergistic retrievals of species-specific extinction profiles (dust, sea salt, black carbon, and water-soluble aerosols) to explicitly optimize the three-dimensional distributions of individual components over East Asia. Results demonstrate that this DA system successfully reconstructs the complex vertical layering of multi-component aerosols. Notably, it effectively corrects severe underestimations of elevated black carbon (BC) plumes, capturing persistent free-tropospheric BC layers over South Asia that traditional models typically miss. Independent validations against ground-based AERONET and AD-Net lidar observations confirm significant improvements not only in total AOT and extinction but also in the single scattering albedo (SSA). By independently adjusting the mass of scattering and absorbing species, the system corrects local biases in aerosol optical properties. Consequently, the optimized component-specific profiles profoundly affect the atmospheric shortwave radiative heating. The elevated BC plumes induces a pronounced mid-tropospheric warming accompanied by a reduction in lower-tropospheric heating due to the attenuation of downward solar radiation. This study highlights the importance of component-specific vertical constraints for accurately assessing aerosol-induced atmospheric heating and its vertical structure.

https://doi.org/10.5194/egusphere-2026-2340
Preprint. Discussion started: 2 June 2026

1 Introduction

Aerosols significantly affect the Earth's energy budget by scattering and absorbing solar shortwave radiation, thereby modulating atmospheric heating rates and radiative effects. Recent research identifies the vertical distribution of aerosols as a dominant driver of uncertainties in these radiative processes (Li et al., 2022). The vertical profile governs the altitude at which solar energy is absorbed and scattered, capable of altering the atmospheric thermal structure (Samset and Myhre, 2011; Samset et al., 2013). Specifically, this profound sensitivity is dictated by the vertically resolved profiles of distinct aerosol components, particularly absorbing species. Elevated absorbing layers over dark surfaces intercept more incoming solar radiation to enhance atmospheric warming, whereas over bright surfaces, their interaction with reflected radiation induces stronger warming in the lower atmosphere (Haywood and Ramaswamy, 1998; Mishra et al., 2015). Consequently, the radiative heating induced by black carbon in the stratosphere can exceed its near-surface effect by over an order of magnitude (Samset and Myhre, 2011). Concurrently, scattering aerosols modulate radiative effect through altitude-dependent interactions with water vapor absorption (Oikawa et al., 2018; Dong et al., 2021). This radiative complexity is substantially amplified by the non-linear mixing of multi-component aerosols. For instance, scattering aerosols positioned beneath absorbing layers significantly enhance net atmospheric absorption and warming (Noh et al., 2016). Furthermore, atmospheric heating exhibits strong non-linear responses to the relative partitioning of these species; a mere ±3% variation in the scattering-to-extinction ratio can perturb the radiative effect by 50% (Loeb and Su, 2010), and multi-component mixing can alter regional radiative effect estimates by up to 100% (Mishra et al., 2015; Zhang et al., 2022). Therefore, neglecting the distinct vertical mechanisms of individual components introduces substantial uncertainties into atmospheric heating assessments. Despite its critical importance, the severe lack of three-dimensional observational data for aerosol speciation currently constrains our ability to quantitatively assess how component-specific vertical structures affect atmospheric heating. Current approaches to characterizing aerosol vertical structure primarily rely on active remote sensing and numerical modelling, yet both exhibit significant limitations. Ground-based lidar networks, such as Asian Dust and aerosol lidar observation Network (AD-Net) and the Micro-Pulse Lidar Network (MPLNET), can provide valuable insights into regional vertical distributions (Welton et al., 2002; Shimizu et al., 2004; Wang et al., 2022). However, the sparse distribution of these stations limits their spatial coverage. Satellite-borne lidars, such as Cloud-Aerosol Lidar with Orthogonal Polarization (CALIOP) and the Cloud-Aerosol Transport System (CATS), can provide high-resolution vertical profiling (Campbell et al., 2010; Proestakis et al., 2019), yet they are constrained by temporal discontinuity. Although numerical models such as Weather Research and Forecasting model coupled with Chemistry (WRF-Chem) offer continuous spatiotemporal coverage, their simulations still frequently deviate from observations due to uncertainties in emission inventories, coarse grid resolutions, and imperfect sub-grid physical parameterizations (Hu et al., 2010; Koffi et al., 2016; Zeng et al., 2020). Consequently, the lack of continuous and three-dimensional observations, combined with inherent model biases, severely restricts the accurate quantification of aerosol vertical structures and their radiative effects.

https://doi.org/10.5194/egusphere-2026-2340
Preprint. Discussion started: 2 June 2026

Data Assimilation (DA) offers a robust strategy to bridge the gap between observations and models. However, traditional DA studies have predominantly focused on assimilating column-integrated Aerosol Optical Thickness (AOT) (Rubin et al., 2017; Di Tomaso et al., 2017; Yumimoto et al., 2018; Chen et al., 2022; Huang et al., 2023) or surface mass concentrations (Peng et al., 2018; Jin et al., 2022). Since these observations lack vertical information, the assimilation system is forced to distribute increments based on the model's background profile, leaving errors in the vertical structure largely uncorrected (Cheng et al., 2019; Ye et al., 2021; Gao et al., 2025; Pang et al., 2025). Recent advances in vertical DA using lidar extinction profiles have proven effective in improving three-dimensional aerosol structures (Zhang et al., 2011; Wang et al., 2022; Escribano et al., 2022) and correcting biases in the boundary layer (El Amraoui et al., 2020). Despite these improvements, a critical gap persists in vertical DA methodologies. Conventional frameworks typically assimilate total aerosol extinction by distributing increments proportionally across different aerosol species, thereby rigidly coupling species abundance to the background model state. This simplification is physically unrealistic, as it neglects the distinct optical properties (e.g., mass extinction efficiencies and single scattering albedos) inherent to different aerosol components. As demonstrated by Tsikerdekis et al. (2021), simply scaling total mass cannot correct structural biases in species-specific optical contributions. Consequently, such DA systems are prone to the misallocation of aerosol mass among different chemical species. For example, the assimilation process may erroneously increase the mass of scattering aerosols to compensate for an underestimation of absorbing species. As highlighted by Yang et al. (2023), relying on a single optical constraint is insufficient to separate the contributions of individual aerosol components. This under-constrained problem ultimately leads to inaccurate vertical profiles of aerosol speciation and introduces subsequent biases in the estimation of aerosol shortwave radiative heating.

The consequences of this under-constrained problem are particularly severe over East Asia. Characterized by intense anthropogenic emissions and frequent natural dust events, this region exhibits a highly diverse aerosol mixture and complex vertical layering (Li et al., 2018). Because strongly absorbing and scattering aerosols frequently co-exist and overlap vertically, just relying on total extinction constraint here significantly exacerbates the misallocation of aerosol species. Consequently, accurately constraining the component-specific vertical profiles in this region is urgently needed to reduce regional radiative uncertainties and better evaluate atmospheric heating rates.

To bridge this gap, we introduce a data assimilation framework explicitly constrained by vertical profiles of specific aerosol components. Unlike traditional approaches, this method leverages species-specific observations to better capture the vertical distribution of individual aerosols, thereby reconstructing the three-dimensional multi-component aerosol structure over East Asia with high accuracy. Beyond structural reconstruction, we quantitatively assess how these optimized vertical profiles govern the radiative response. This study presents a novel pathway for refining component-specific vertical structures via DA, providing critical insights into aerosol-induced atmospheric heating, which is necessary for investigations into regional thermodynamic and dynamic feedbacks. The paper is organized as follows: Section 2 details the observational datasets and modelling system, Section 3 describes the component-constrained DA methodology, Section 4 evaluates the optimized aerosol fields and their radiative implications, and Section 5 summarizes the conclusions and discusses broader implications.

https://doi.org/10.5194/egusphere-2026-2340
Preprint. Discussion started: 2 June 2026

2 Numerical Model and Observational Data

2.1 Forward model

The forward model employed in this study is the Weather Research and Forecasting model coupled with Chemistry (WRF-Chem, version 4.4). The model domain covers East Asia with a 25 km horizontal resolution and utilizes 34 terrain-following sigma levels extending from the surface to 10 hPa. The model physics configuration employs the Thompson microphysics scheme to explicitly account for aerosol-cloud interactions (Thompson et al., 2008). Radiative transfer processes are computed using the Rapid Radiative Transfer Model for GCMs (RRTMG) for both shortwave and longwave bands (Iacono et al., 2008). Boundary layer dynamics are represented by the Yonsei University (YSU) scheme (Hong et al., 2006), coupled with the Unified Noah Land Surface Model (Chen and Dudhia, 2001). Convection is parameterized via the Grell-Freitas ensemble scheme (Grell and Freitas, 2014). The Goddard Chemistry Aerosol Radiation and Transport (GOCART) aerosol module (chem_opt = 300) is used to simulate major tropospheric aerosol species, including sulfate, mineral dust, sea salt, organic carbon (OC), and black carbon (BC) (Chin et al., 2002). Initial and boundary meteorological fields are provided by the ERA5 reanalysis dataset (Hersbach et al., 2020), and the meteorological fields are simulated as a free run without grid nudging. Dust and sea salt emissions are calculated online as a function of surface wind speed. Anthropogenic emissions are mapped from the HTAPv3 mosaic emission inventory for the year 2018 (Crippa et al., 2023), while biomass burning emissions are provided by the Fire INventory from NCAR (FINN) version 2.5 (Wiedinmyer et al., 2023), incorporating a plume-rise parameterization to account for injection heights (Freitas et al., 2007). To capture radiative effects, the model is configured with aerosol-radiation feedback enabled. While the aerosol mass simulation follows the original GOCART scheme (Chin et al., 2002), the optical calculations employ the microphysical assumptions inherent to the Community Radiative Transfer Model (CRTM). Aerosols are parameterized as externally mixed spherical particles with lognormal size distributions. For Mie scattering calculations, the effective radius, geometric standard deviation, and complex refractive index of each species are explicitly defined according to the CRTM GOCART-GEOS5 configuration (Lu et al., 2022). These microphysical parameters govern the baseline optical properties and hygroscopic growth, establishing the physical foundation for the observation operator detailed in Section 3.1.

2.2 Observation data

2.2.1 CALIOP-MODIS aerosol component retrieval

This study assimilates a global three-dimensional aerosol composition dataset developed by Kudo et al. (2023). This dataset is generated using a synergistic retrieval algorithm that combines attenuated backscatter measurements from the Cloud-Aerosol Lidar with Orthogonal Polarization (CALIOP) and passive radiance measurements from the Moderate Resolution Imaging Spectroradiometer (MODIS). It provides vertical profiles of aerosol extinction coefficients, backscatter coefficients, depolarization ratios, and volume concentrations for four specific aerosol components: sea salt (SS), dust (DS), black carbon (BC), and water-soluble (WS).

https://doi.org/10.5194/egusphere-2026-2340
Preprint. Discussion started: 2 June 2026

To generate representative "super-observations" for assimilation, strict quality control and aggregation procedures are applied to the CALIOP-MODIS original orbital retrievals. The data are mapped onto the 25 km WRF horizontal grid by a two-step statistical screening. First, outliers are removed by excluding pixel-level retrievals falling outside one standard deviation of the grid mean. Second, data are retained only for grid cells with sufficient sampling (N > 3) and a coefficient of extinction variation below 0.5, thereby filtering out high sub-grid variability (Zhang and Reid, 2006; Schutgens et al., 2017; Cheng et al., 2019). The screened extinction profiles are then vertically regridded to WRF layers using layer-weighted averaging, requiring a minimum vertical coverage of 20%. The observational uncertainty ϵ_o is calculated as $\epsilon_o = \sqrt{\epsilon_{inst+retri}^2 + \epsilon_{rep}^2}$, where $\epsilon_{inst+retri}$ is the instrumental error and ϵ_{rep} is the representativeness error. Because the retrieval algorithm does not explicitly provide retrieval uncertainties, 10% of the observed aerosol extinction is employed as an empirical proxy to implicitly account for the baseline instrumental and retrieval errors. The representativeness error is derived from the standard deviation of the sub-grid high-resolution retrievals within the 25 km WRF grid cell. Furthermore, the observation error covariance matrix is assumed to be diagonal. This assumption neglects vertical error correlations and cross-covariances between different aerosol species for computational simplicity and to maintain consistency with the variable localization strategy. Finally, hourly aerosol extinction profiles and uncertainties for the four aerosol components are generated at the model resolution for data assimilation. Figure 1 shows the spatial distributions of the gridded AOT integrated from observed extinction coefficients, along with the observation counts for each component used for assimilation during March 5-25, 2021.

https://doi.org/10.5194/egusphere-2026-2340
Preprint. Discussion started: 2 June 2026

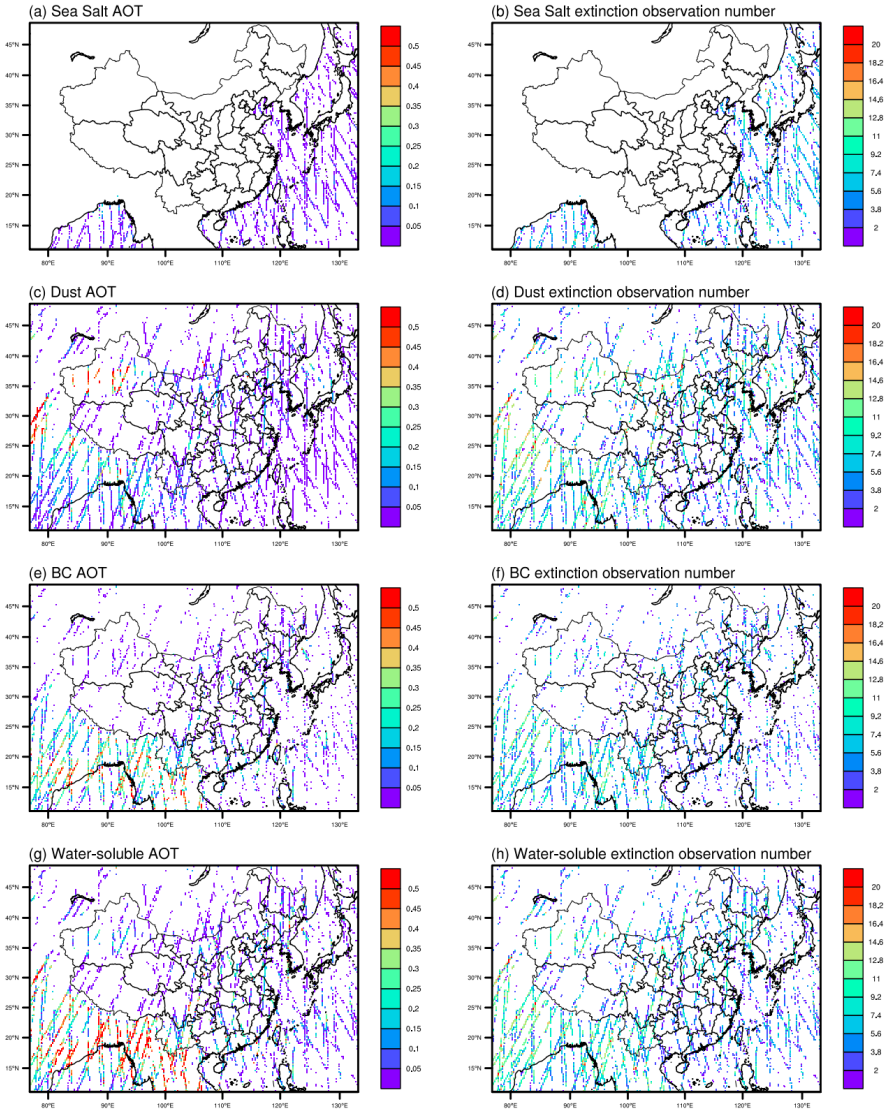

Figure 1. Spatial distributions of the gridded Aerosol Optical Thickness (AOT) integrated from observed extinction coefficients, and the corresponding observation counts for each aerosol component used for assimilation (March 5-25, 2021).

2.2.2 AERONET

The AErosol RObotic NETwork (AERONET; http://aeronet.gsfc.nasa.gov/) provides globally ground-based measurements of aerosol properties (Holben et al., 1998). In this study, AERONET data are used as an independent dataset for the validation of column-integrated aerosol properties. We utilized both AOT and SSA products from the Version 3 (V3) Level 2.0 (quality-assured) dataset (Dubovik and King, 2000; Giles et al., 2019; Sinyuk et al., 2020). Specifically, AOT data are

https://doi.org/10.5194/egusphere-2026-2340
Preprint. Discussion started: 2 June 2026

derived from the direct sun algorithm, while SSA retrievals are sourced from the inversion product. AOT at 532 nm is calculated by spectrally interpolating measurements from the 440 and 675 nm channels, while SSA at 532 nm is interpolated using data from the 440 and 675 nm. To match the model temporal resolution, high-frequency observations are averaged within a ±30-minute window centered on each hour.

2.2.3 AD-Net

Ground-based lidar measurements from the Asian Dust and Aerosol Lidar Observation Network (AD-Net) (http://www-lidar.nies.go.jp/AD-Net, Sugimoto et al., 2003; Shimizu et al., 2004) were used to evaluate the simulated vertical aerosol distributions. We utilized standard AD-Net products, which derive 532 nm aerosol extinction coefficient via the Fernald inversion method (Fernald, 1984). Additionally, the particle depolarization ratio is used to partition total extinction into dust (non-spherical) and spherical components (Shimizu et al., 2004; Nishizawa et al., 2007). To match the model temporal resolution, quality-controlled 15-minute observations were averaged hourly (±30 minutes). For vertical collocation, the observed profiles are linearly interpolated to the model hybrid-sigma levels.

3 Component-resolved 4D-LETKF system

In this study, we developed a component-resolved four-dimensional local ensemble transform Kalman filter (4D-LETKF) data assimilation system with spatial and observational constraints for WRF-Chem (Fig. 2). While based on a global aerosol assimilation system for the NICAM-SPRINTARS model (Cheng et al., 2019), this system has been substantially extended to assimilate component-specific vertical extinction profiles rather than total aerosol extinction. To assimilate the multi-species aerosol vertical observations, we develop the new observation operators and implement spatiotemporal and variable localization schemes. Furthermore, severe model underestimations or missed aerosol events often result in near-zero background variance. To address this, we introduce a background correction strategy that maintains sufficient ensemble spread, allowing the system to effectively assimilate the observations and reconstruct unsimulated aerosol events.

https://doi.org/10.5194/egusphere-2026-2340
Preprint. Discussion started: 2 June 2026

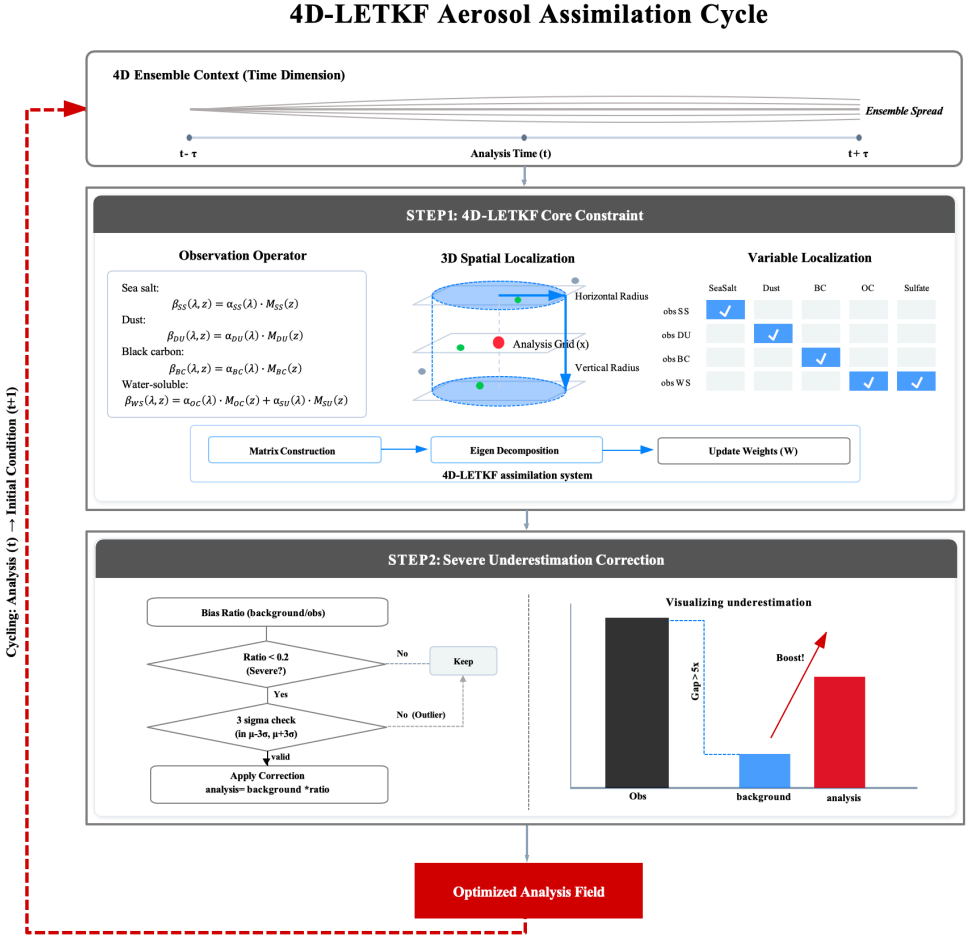

Figure 2. Schematic illustrating the component-resolved 4D-LETKF system with spatial and observational constraints.

3.1 Component-specific observation operator

Building upon the 4D-LETKF framework, the efficacy of the assimilation system relies heavily on the precise definition of the state vector and its mapping to observation space. For this component-resolved assimilation, the state vector consists of the mixing ratios of 14 GOCART aerosol species: sulfate, hydrophobic and hydrophilic black carbon (BC), hydrophobic and hydrophilic organic carbon (OC), dust in five size bins, and sea salt in four size bins. To link these model states with the component-resolved lidar retrievals, we develop an observation operator that establishes a physical correspondence between the simulated aerosol species and four components of aerosol extinction observations. Unlike traditional operators that aggregate species into bulk fine and coarse modes, our approach explicitly maps individual model variables to their corresponding component observations. Specifically, the simulated mass concentrations of sea salt (M_{SS}) and dust (M_{DU}) are mapped directly to their respective extinction coefficients (β_{SS} and β_{DU}), and BC mass concentration (M_{BC}) is aggregated to

https://doi.org/10.5194/egusphere-2026-2340
Preprint. Discussion started: 2 June 2026

calculate β_{BC}. The observed water-soluble extinction (β_{WS}) is defined as the combined contribution from sulfate (M_{SU}) and organic carbon (M_{OC}), formulated as:

$$\beta_{WS}(\lambda, z) = \alpha_{OC}(\lambda) \cdot M_{OC}(z) + \alpha_{SU}(\lambda) \cdot M_{SU}(z). \quad (195)$$

where α represents the mass extinction efficiency (MEE). To rigorously account for the hygroscopic growth of hydrophilic aerosols, the MEEs are not treated as constants but are dynamically calculated as a function of the model-simulated ambient relative humidity (RH). Specifically, these RH-dependent optical properties are explicitly derived from the Community Radiative Transfer Model (CRTM) GOCART-GEOS5 aerosol lookup tables and spectrally interpolated to the observation wavelength of 532 nm. This dynamic mapping ensures a physically consistent conversion from aerosol mass to optical space under varying meteorological conditions.

3.2 Localization strategy

We implemented a dual localization framework to mitigate sampling errors inherent in a finite ensemble size and to eliminate spurious correlations. First, spatiotemporal localization restricts the observation influence using a Gaussian function based on the four-dimensional distance:

$$f(r) = exp\left(-\frac{r_h^2}{2\sigma_h^2} - \frac{r_v^2}{2\sigma_v^2} - \frac{\Delta t^2}{2\sigma_t^2}\right),$$

where r_h, r_v, and Δt represent the horizontal, vertical, and temporal distances of the observations from the local patch center, respectively. The horizontal localization length σ_h, vertical localization length σ_v, and temporal localization scale σ_t are set to 75 km, 1 model layer and 0.01, respectively. Following Miyoshi et al. (2007), we approximate the Gaspari and Cohn (1999) function by truncating Gaussian tails at $r = 2 \cdot \sqrt{10/3} \cdot \sigma$, discarding observations beyond this cutoff.

Second, we applied component-wise variable localization to prevent unphysical cross-updates between different chemical components. By enforcing a block-diagonal structure on the background error covariance, observations of dust, sea salt, and black carbon are restricted to update only their corresponding mass concentrations. In contrast, water-soluble extinction observations are permitted to simultaneously update both sulfate and OC, consistent with the observation operator. This strict variable localization ensures that unrelated species remain statistically uncorrelated, thereby preserving the physical and chemical consistency of the analysis field after data assimilation.

3.3 Background correction strategy based on spatial and observational constraints

In our system, a 20 member background ensemble is generated by applying spatiotemporal lognormal perturbations to the aerosol emissions (Cheng et al., 2019). However, severe model underestimations or completely missed aerosol events often result in a near-zero background ensemble mean and spread. Under such conditions, the standard LETKF would yield a near-zero Kalman gain, effectively ignoring the observations. To mitigate this, we implement a background correction scheme based on spatial and observational constraints prior to the assimilation step. For each analysis grid point, the scheme identifies valid observations within a specified localization radius and applies a distance-dependent localization function, f_i,

https://doi.org/10.5194/egusphere-2026-2340
Preprint. Discussion started: 2 June 2026

to weight their contributions. We define a localized weighted bias ratio, R_{corr}, which quantifies the discrepancy between the observations y_i^o and the background ensemble mean $H(x^b)_i$ within the local domain:

$$R_{corr} = \frac{\sum_{i=1}^{N_{obs}} \sqrt{f_i} \frac{H(x^b)_i}{y_i^o}}{\sum_{i=1}^{N_{obs}} \sqrt{f_i}},$$

where N_{obs} represents the number of valid observations within the localization radius. To ensure statistical robustness and filter out noise, the correction is triggered only when strict criteria are met: the number of local observations must exceed a minimum threshold ($N_{obs} > 3$), and the calculated ratio must fall within three standard deviations of the local statistics (3-sigma rule) to exclude outliers. In regions where the weighted ratio R_{corr} falls below an empirical threshold of 0.2, thereby representing severe underestimation, the background ensemble members are rescaled by dividing by this factor. Crucially, when this correction is triggered, the rescaled ensemble directly serves as the analysis field, bypassing the LETKF assimilation step for that specific location. Conversely, in regions where this correction is not triggered, the system proceeds with the standard LETKF assimilation to optimally combine the background and observations. This conditional strategy effectively corrects severe negative biases, where the standard filter would otherwise fail due to near-zero background spread, while preserving the physical consistency of the ensemble.

3.4 Experimental design

To evaluate the impact of data assimilation, two experiments are conducted: a free run without assimilation (FR) and an assimilation run (DA) assimilating the specific aerosol component extinction coefficients. Both experiments spanned from March 1 to March 25, 2021, with the first five days serving as a spin-up period. Furthermore, to mitigate filter divergence and maintain adequate ensemble spread, a fixed multiplicative inflation factor of 1.1 is applied to the background ensemble perturbations, following Sekiyama et al. (2010).

4 Results

This section presents a comprehensive evaluation of the 4D-LETKF aerosol component assimilation system, systematically assessing its performance from the reconstruction of aerosol three-dimensional structure to its ultimate impact on radiative properties. Section 4.1 presents a self-validation using the assimilated CALIOP observations to verify the system's ability in reconstructing the three-dimensional distributions of individual aerosol components. To ensure the robustness of this assimilation system, Section 4.2 conducts an independent validation using ground-based AERONET and NIES Lidar measurements. This step evaluates the system's capability to reproduce aerosol fields, highlighting how asynchronous assimilation improves the spatiotemporal evolution of aerosol distributions. Beyond bulk optical depth, Section 4.3 further compares the simulated single scattering albedo (SSA) against independent AERONET retrievals, demonstrating the effectiveness of component-specific assimilation in adjusting aerosol scattering and absorption characteristics. Finally, Section 4.4 quantifies the impact of optimized aerosol analysis fields on the vertical profiles of the aerosol radiative heating

https://doi.org/10.5194/egusphere-2026-2340
Preprint. Discussion started: 2 June 2026

rates. To quantify the model performances, statistical metrics including the bias (BIAS), root mean square error (RMSE), and correlation coefficient (CORR) are calculated between the simulations and observations (Boylan and Russell, 2006; Willmott et al., 2012; Yumimoto et al., 2017).

4.1 Reconstruction of three-dimensional aerosol composition

In this section, we first evaluate the model performance against the assimilated aerosol component extinction coefficients at 532 nm as an internal consistency check (Benedetti et al., 2009). Figure 3 presents scatter density plots comparing the simulated aerosol extinction coefficients from the FR and DA experiments against CALIOP observations for four aerosol components: sea salt, dust, black carbon (BC), and water-soluble (WS) aerosols. As shown in Figs. 3a-d, the FR experiment exhibits a systematic underestimation across all aerosol components. A prominent feature of this negative bias is a high-density region where simulated extinction coefficients approach zero, indicating that the model completely misses aerosol events clearly captured by CALIOP observations. This deficiency is most pronounced for BC (Fig. 3c), where the simulation entirely failed to capture the observed spatio-temporal variations, yielding a notably low CORR of 0.10. Compared with the spatial distributions of the CALIOP observations, it is evident that these elevated BC extinction values are predominantly concentrated over South Asia (Fig. 1). The severe omission of these aerosol plumes in FR experiment demonstrates the background model's inability to represent intense BC emissions and accumulation processes, likely due to significantly underestimated sources in the emission inventories or deficiencies in vertical transport. The implementation of the 4D-LETKF assimilation system (Figs. 3e-h) significantly enhances model performance, effectively mitigating the systematic underestimation observed in FR experiment across all components. For dust, the DA experiment yields a substantial correction (with the CORR increasing from 0.33 to 0.79 and the RMSE decreasing from 0.090 to 0.054), optimizing the three-dimensional structure of dust aerosols especially in the Taklamakan Desert and Thar Desert (Fig. 1). Similarly, the scatter density distribution of WS aerosols becomes markedly more aligned with the 1:1 line (CORR improving from 0.41 to 0.79 and RMSE decreasing from 0.161 to 0.094), indicating an effective correction of secondary aerosol mass concentration. For sea salt, the assimilation effectively reduces the statistical spread (CORR increasing from 0.33 to 0.69 and RMSE decreasing from 0.033 to 0.022), mitigating random errors driven by uncertainties in sea salt emission parameterizations and marine surface wind fields. For BC, the DA experiment increases the CORR from 0.10 to 0.59 and partially captures the high concentration pollution plumes over South Asia (Fig. 1). However, this improvement remains limited compared to other aerosol species, particularly at high concentrations. This limitation is directly due to the severe negative bias in the background field, exposing a fundamental constraint of ensemble-based assimilation: when the forward model fails to simulate a process due to severe structural errors (e.g., missing emissions or failed vertical lofting), the background ensemble spread approaches zero. Consequently, the assimilation system cannot generate sufficient background error covariance to effectively draw the analysis toward the observations. Although our system includes a correction procedure based on spatial and observational constraints to mitigate severe underestimation, it cannot fully compensate for these fundamental model deficiencies. Therefore, while data assimilation effectively corrects model states given a reasonable background, accurate

https://doi.org/10.5194/egusphere-2026-2340
Preprint. Discussion started: 2 June 2026

emission inventories and physical parameterizations remain indispensable for reliably simulating aerosol variations. Furthermore, it is worth noting that the relatively larger BIAS and lower CORR for BC compared to other species (Fig. 3g) can be partially attributed to the inherent discrepancies in microphysical assumptions between the model and the retrieval algorithm. The GOCART model assumes externally mixed pure BC, whereas the CALIOP-MODIS retrieval treats BC as internally mixed with other substances in a core-shell structure. This difference in mixing state significantly alters the assumed optical properties, introducing an unavoidable representativeness error when comparing the simulated and retrieved BC extinctions.

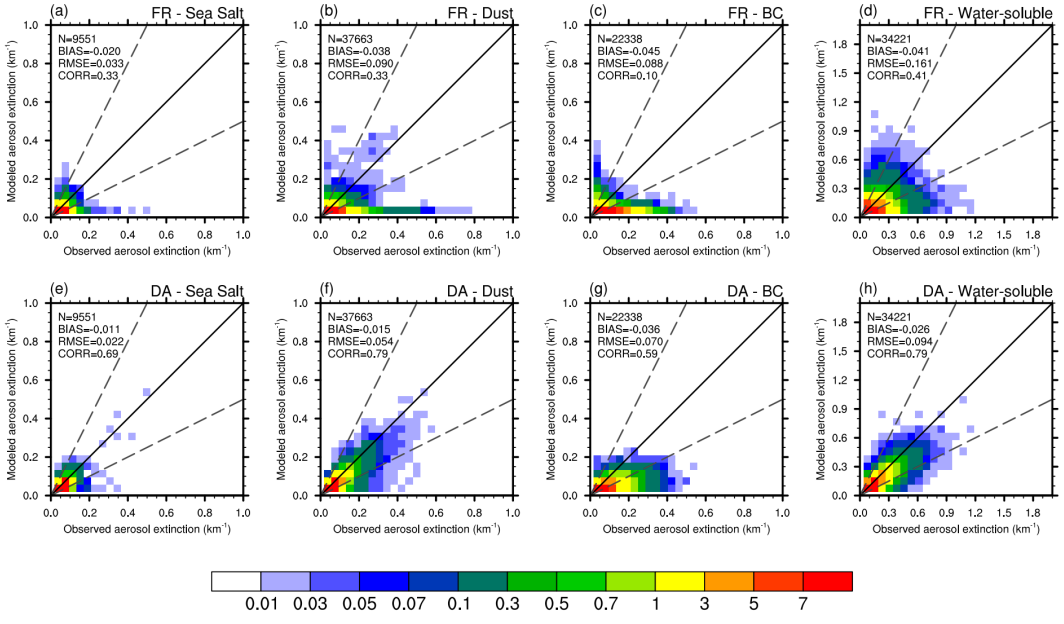

Figure 3. Density scatter plots comparing the modeled extinction coefficients (km^{-1}) against observations for (a, e) sea salt, (b, f) dust, (c, g) black carbon, and (d, h) water-soluble aerosols. The top row (a-d) represents the FR experiment, while the bottom row (e-h) shows the results from the DA experiment. The color scale indicates the data density. The solid black line represents the 1:1 line while the dashed lines represent the 2:1 and 1:2 lines. Statistical metrics (N: sample size, BIAS: bias, RMSE: root mean square error, CORR: correlation coefficient) are provided in each panel. The statistics are calculated using all valid data points within East Asia (shown in Fig. 1) from the surface up to 12 km altitude.

Figure 4 compares the domain-averaged vertical profiles of aerosol extinction coefficients. The FR experiment systematically underestimates the extinction of all four species across all altitudes. Furthermore, while the FR experiment captures the general vertical distribution pattern of dust, it fails to reproduce the observed vertical structures of the other three components. The DA experiment, however, effectively reconstructs these vertical profiles and substantially reduces the negative biases. Specifically, for dust and water-soluble aerosols, the profiles in DA experiment closely match the observations, yielding CORR of 1.00 and substantially reduced RMSEs. For sea salt, the FR simulation produces a false

https://doi.org/10.5194/egusphere-2026-2340
Preprint. Discussion started: 2 June 2026

minimum at approximately 0.5 km instead of the observed near-surface maximum. The DA experiment corrects this profile, properly capturing the low-level accumulation. Regarding BC, the FR profile decreases monotonically with height, completely missing an observed elevated layer peaking at around 6 km. As indicated by the spatial distribution of BC AOT (Fig. 1), this mid-tropospheric peak is primarily driven by intense pollution plumes originating from the Indian subcontinent, which are subsequently lofted into the free troposphere. Chemical transport models frequently fail to reproduce such elevated BC layers due to inherent uncertainties in bottom-up emission inventories and imperfect sub-grid convective parameterizations. Consequently, the presence of these persistent free-tropospheric BC layers over the Indian subcontinent has historically been documented almost exclusively through sparse in-situ profiling using high-altitude balloons and aircraft (Babu et al., 2011; Sunilkumar et al., 2025). The successful reconstruction of this lofted BC plume by the DA experiment (improving the CORR from 0.26 to 0.95) represents a substantial advancement. It underscores the capability of the component-resolved assimilation system to mitigate systematic biases originating from emission deficiencies and to accurately capture complex vertical transport and accumulation processes in the free troposphere. Despite the structural improvement, DA experiment still underestimates the peak magnitude of the BC extinction. Interestingly, the FR simulation produces higher BC extinction near the surface compared to the DA experiment (Fig. 4c). This suggests that the failure to capture the 6 km BC peak is not primarily due to underestimated total emissions, but rather attributable to deficiencies in the model's vertical transport mechanisms or an underrepresentation of the biomass burning plume injection heights. Because the background ensemble spread at this elevated altitude drops to near zero, the assimilation system is difficult to reproduce the absolute magnitude of the lofted plumes.

https://doi.org/10.5194/egusphere-2026-2340
Preprint. Discussion started: 2 June 2026

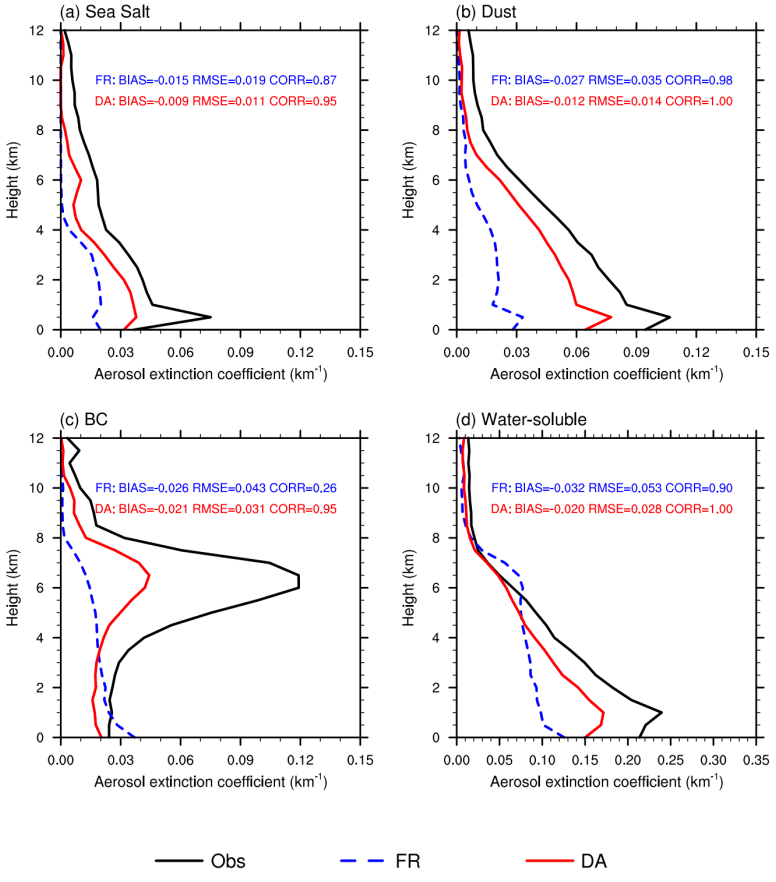

Figure 4. Vertical distribution of extinction coefficients (km^{-1}) for (a) sea salt, (b) dust, (c) black carbon, and (d) water-soluble aerosols. The black solid lines represent the assimilated CALIOP observations. The blue dashed lines and red solid lines denote the results from the FR and DA experiments, respectively. Statistical metrics (BIAS, RMSE, and CORR) calculated for the vertical profiles are listed in each panel. The profiles represent the domain-averaged values over East Asia (shown in Fig. 1).

Figure 5 further quantifies these vertical discrepancies by integrating the absolute aerosol extinction and fractional contributions across four altitude layers. Consistent with Figure 4, the FR experiment (Fig. 5b) systematically underestimates the total aerosol extinction at all altitudes compared to CALIOP observations (Fig. 5a). The DA experiment (Fig. 5c) effectively mitigates this negative bias, particularly in the lower-to-mid troposphere (0-6 km), although a slight underestimation persists in the mid-troposphere. Beyond absolute extinction, the fractional analysis (Fig. 5d-f) highlights the capability of data assimilation to correct the vertical aerosol composition. A major deficiency in the FR simulation (Fig. 5e) is the spurious dominance of water-soluble aerosols across all altitude layers, which artificially suppresses the BC and dust fractions. The DA experiment successfully corrects this vertical partitioning. Specifically, in the lower free troposphere (1-3 km), the DA experiment reproduces the observed balanced contribution among dust, BC, and water-soluble aerosols,

https://doi.org/10.5194/egusphere-2026-2340
Preprint. Discussion started: 2 June 2026

eliminating the water-soluble overestimation in the FR simulation. In the mid-troposphere (3-6 km), observations indicate that BC becomes the dominant aerosol type (approximately 50%). The FR simulation misses this feature, maintaining an artificially high water-soluble fraction (up to 78%). By assimilating the observations, the DA experiment successfully captures the elevated BC fraction and reduces the excessive water-soluble contribution, yielding a composition profile consistent with CALIOP observations. Furthermore, while the FR experiment severely underestimates the dust fraction (remaining below 15% at all altitudes), the DA experiment effectively reproduces the observed substantial dust contributions (20–35%) throughout the vertical column. Overall, these results demonstrate that the DA method can effectively constrain both the total aerosol loading and the vertical partitioning of different aerosol species.

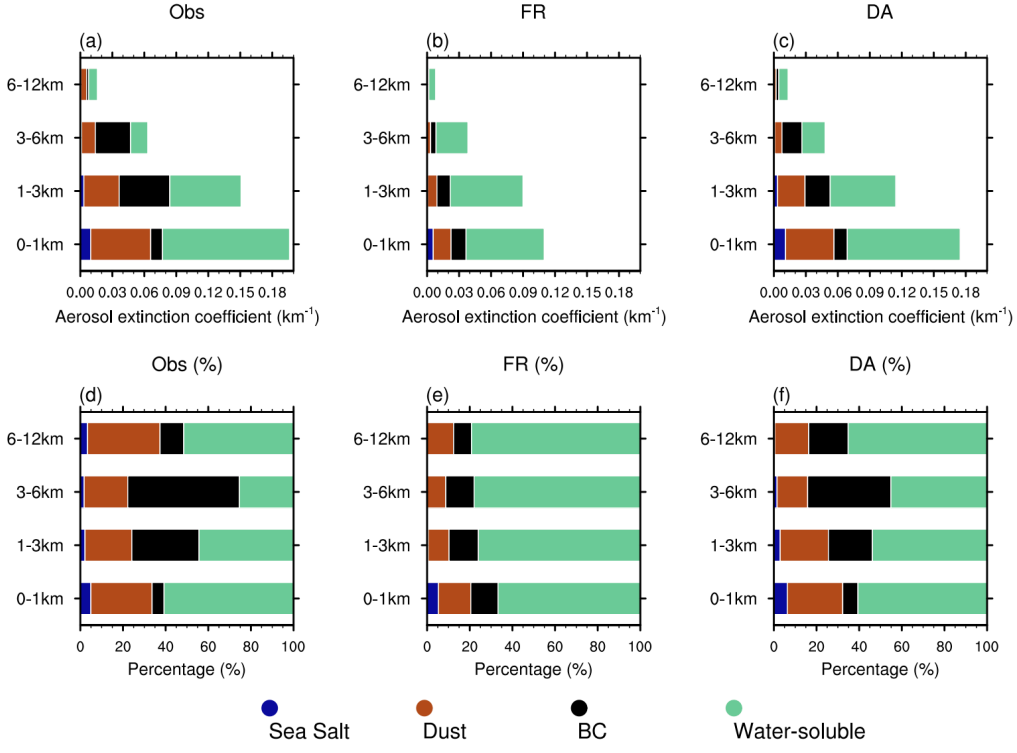

Figure 5. Comparison of aerosol extinction coefficients (km^{-1}) observed by CALIOP observations, simulated by FR, and DA experiments in four vertical layers (0-1 km, 1-3 km, 3-6 km, and 6-12 km). (a-c) Mean aerosol extinction coefficients for each layer. (d-f) Fractional contribution (%) of each aerosol species to the total extinction. The colors represent different aerosol components: sea salt (blue), dust (brown), black carbon (black), and water-soluble (green).

4.2 Spatiotemporal assessment using independent AERONET and Lidar observations

In this section, the simulated AOT is compared with independent ground-based AERONET observations to validate the assimilation system. Figure 6 presents the density scatter plots and the frequency distribution of AOT deviations for all available AERONET stations during the study period. The FR experiment exhibits a systematic underestimation of AOT,

https://doi.org/10.5194/egusphere-2026-2340
Preprint. Discussion started: 2 June 2026

characterized by a negative BIAS of -0.278, an RMSE of 0.521, and a CORR of 0.573. The DA experiment effectively mitigates this negative bias, reducing the BIAS to -0.208 and the RMSE to 0.488, while improving the CORR to 0.626. The frequency distribution of AOT deviations further confirms this improvement. The DA experiment narrows the error distribution, yielding a higher frequency of near-zero deviations (e.g., the fraction within the -0.10<deviation<0.10 range increases from 23.36% to 28.10%) and notably reducing the frequency of large positive deviations (>0.5) from 21.58% to 16.70%.

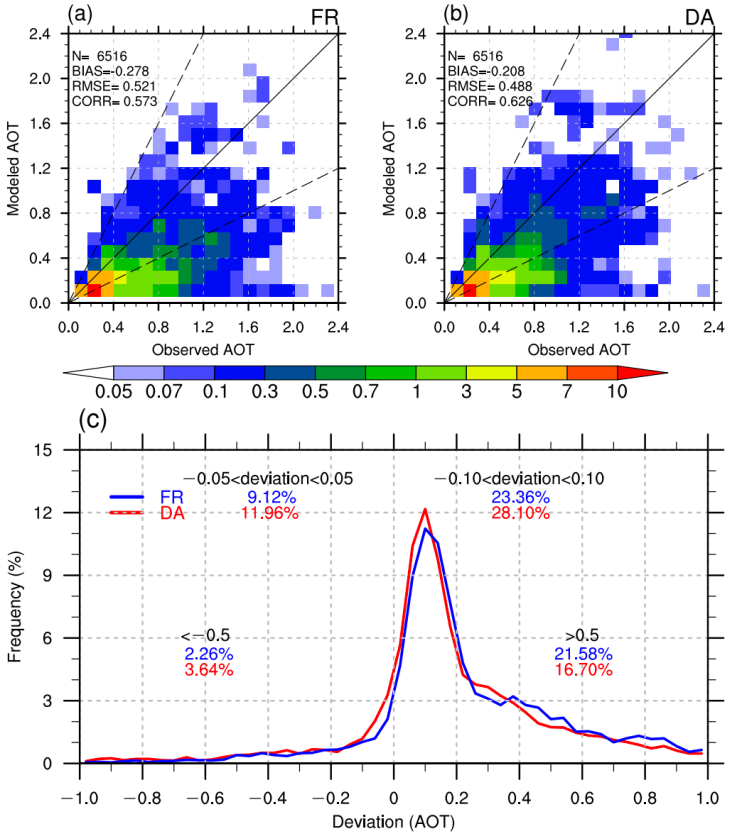

Figure 6. Density scatter plots comparing the modeled AOT against AERONET observations for (a) the FR and DA experiments. The color scale indicates the data density. The solid black line represents the 1:1 line while the dashed lines represent the 2:1 and 1:2 lines. Statistical metrics (N: sample size, BIAS: bias, RMSE: root mean square error, CORR: correlation coefficient) are provided. (c) Frequency distribution of AOT deviations (Modeled minus Observed). The blue and red lines denote the results from the FR and DA experiments, respectively. The percentages indicate the proportion of samples falling within specific deviation ranges.

The spatial distribution of the assimilation impact is illustrated in Figure 7. While observations show high aerosol loadings over South Asia, the FR experiment displays widespread negative biases and high RMSE values across most sites. Figures 7d and 7e highlight the percentage improvements of the DA experiment relative to the FR simulation in terms of absolute

https://doi.org/10.5194/egusphere-2026-2340
Preprint. Discussion started: 2 June 2026

BIAS and RMSE, respectively. Statistically, the DA experiment yields lower RMSE values at 42 out of 59 sites (71.19%) and reduces the absolute BIAS at 54 sites (91.53%).

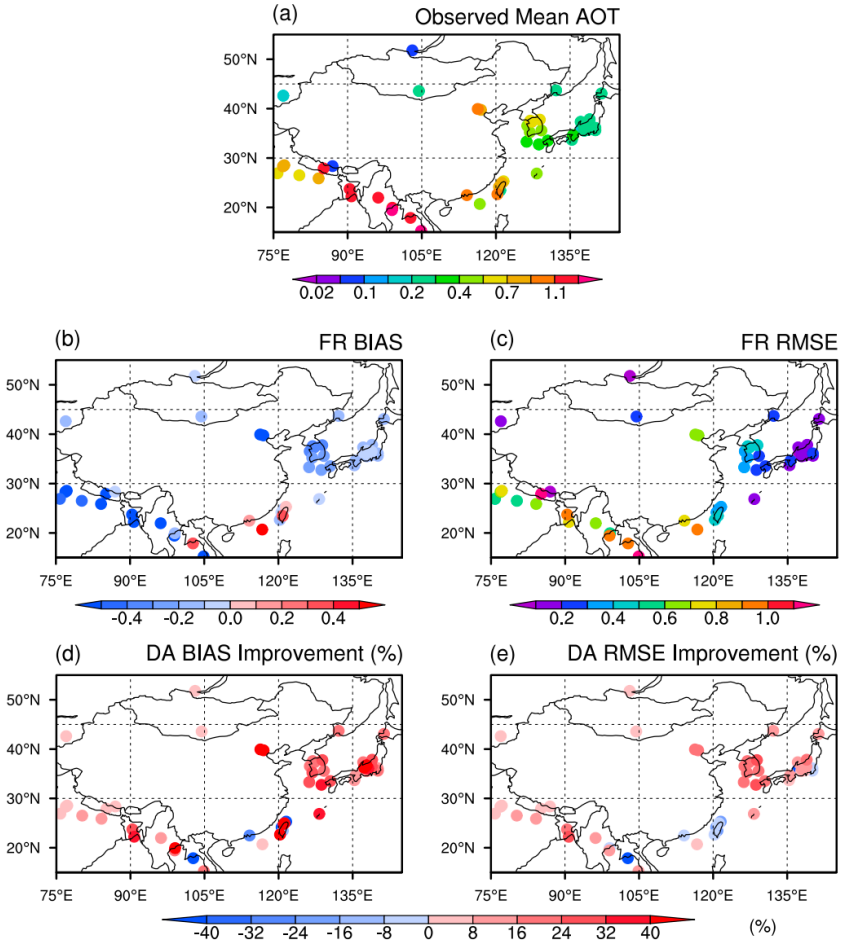

Figure 7. Spatial distributions of observed AOT and model evaluation metrics against AERONET observations. (a) The observed mean AOT averaged over the study period. (b) Mean Bias (BIAS) and (c) Root Mean Square Error (RMSE) for FR experiment. The colored circles represent the locations of observation sites, with the color scale indicating the magnitude of the variable. (d) The percentage improvement of the DA experiment relative to the FR simulation in terms of absolute BIAS (defined as $\frac{(|BIAS_{FR}|-|BIAS_{DA}|)}{|BIAS_{FR}|} \times 100\%$), and (e) the percentage improvement in RMSE (defined as $\frac{(RMSE_{FR}-RMSE_{DA})}{RMSE_{FR}} \times 100\%$).

Time series analysis at four representative AERONET stations (Figure 8) further demonstrates the temporal consistency of the DA improvements. Regionally, DA successfully corrects the FR's underestimation of high-AOT events in source regions (e.g., Beijing-CAMS and Dhaka_University) while maintaining strong agreement with ground observations in downwind areas (e.g., Fukuoka and Gangneung_WNU). This confirms that assimilation effectively constrains both local aerosol

https://doi.org/10.5194/egusphere-2026-2340
Preprint. Discussion started: 2 June 2026

concentrations and long-range transport. Crucially, these improvements highlight the capability of the assimilation system to overcome the limitations of the satellite's narrow swath and sparse sampling. Through horizontal localization, the observational information is effectively spread spatially to update adjacent grid cells. Furthermore, the optimized initial conditions are continuously propagated spatiotemporally, driven by atmospheric transport and model dynamics. Consequently, the assimilation benefits extend well beyond specific CALIOP footprints and overpass times, yielding a domain-wide enhancement in the spatiotemporal representation of aerosols.

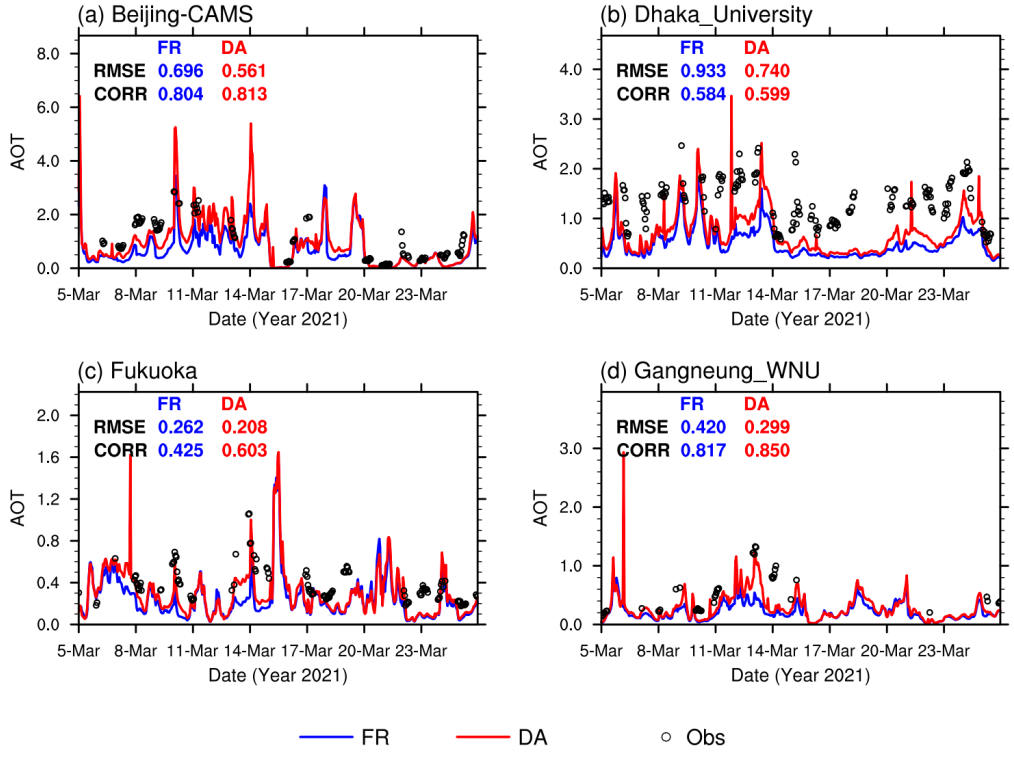

Figure 8. Time series comparison of AOT between model simulations and AERONET observations at four selected sites during March 5-25, 2021. The panels show results for (a) Beijing-CAMS, (b) Dhaka University, (c) Fukuoka, and (d) Gangneung-WNU. The blue and red solid lines represent the time evolution of AOT from the FR and DA experiments, respectively, while the black open circles denote the corresponding AERONET observations. Statistical metrics, including the Root Mean Square Error (RMSE) and Correlation Coefficient (CORR), are inset within each panel for both experiments.

Figure 9 compares the simulated time-height cross-sections of aerosol extinction coefficients with independent ground-based lidar measurements at the AD-Net Fukue site (32.75°N, 128.68°E) from 5 to 25 March 2021. Observations reveal a complex vertical structure featuring intense aerosol layers predominantly confined below 1 km, accompanied by episodic elevated transport plumes extending up to 2-4 km (e.g., during 9-11 and 13-16 March). The FR experiment severely underestimates the extinction magnitude across all layers, missing both the intense near-surface aerosol loadings and the elevated plumes. In

https://doi.org/10.5194/egusphere-2026-2340
Preprint. Discussion started: 2 June 2026

405 contrast, the DA experiment significantly reduces these negative biases, successfully reproducing the high extinction in the lower troposphere and the vertical evolution of the transport episodes. Notably, as CALIOP tracks are sparse over Japan (Figure 1), this improvement at the downwind Fukue site is not driven by local data assimilation. Instead, it results from the optimized three-dimensional aerosol initial fields over the upstream Asian continent. Unlike column-integrated AOT assimilation, assimilating speciated CALIOP profiles provides essential vertical and compositional constraints. The accurate
410 reproduction of the vertical structure at Fukue confirms that optimizing upstream initial conditions effectively improves the simulation of subsequent long-range transport and downwind aerosol distributions.

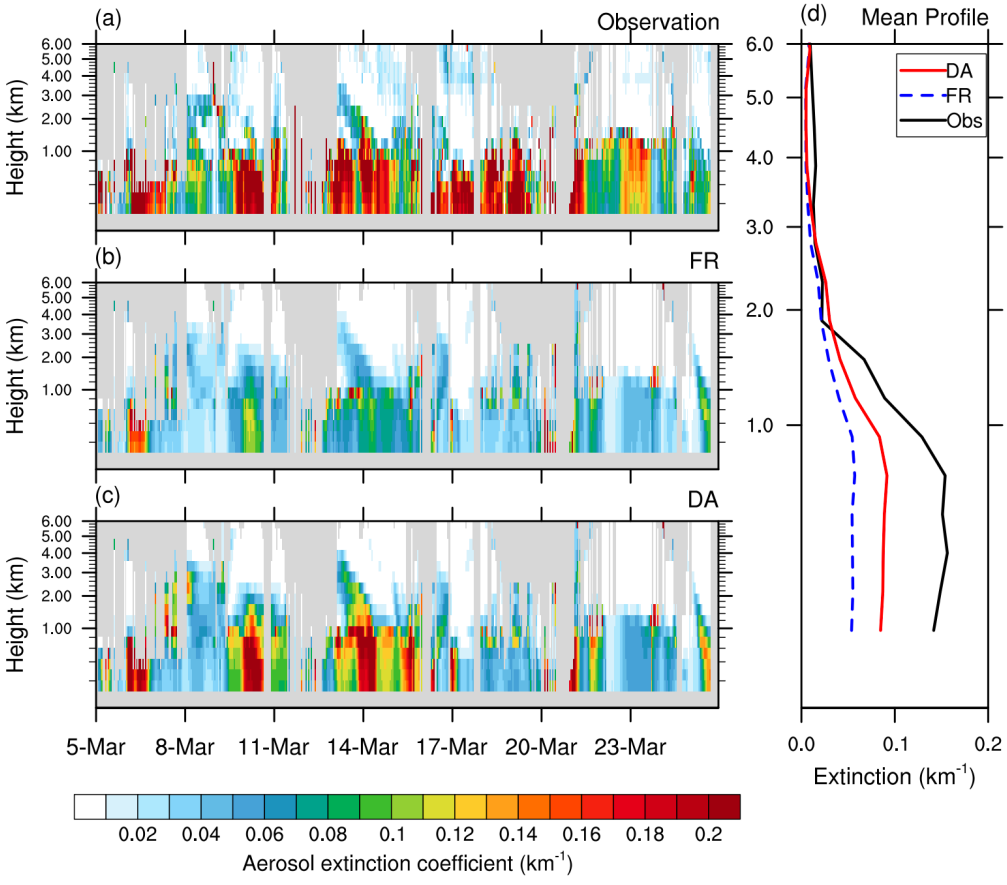

Figure 9. Comparisons of total observed aerosol extinction coefficients from AD-Net (a) and simulated coefficients for FR (b) and DA (c) experiments from 5 to 25 March 2021 at Fukue site (32.75N, 128.68E). (d) The time-averaged
415 **vertical profiles of aerosol extinction coefficients for the period.**

4.3 Improvement in single scattering albedo and absorption

Figure 10 compares the simulated single scattering albedo (SSA) with independent AERONET observations. Interestingly, while the model background generally underestimates the black carbon fraction over the broader domain (as indicated by the

https://doi.org/10.5194/egusphere-2026-2340
Preprint. Discussion started: 2 June 2026

CALIOP comparisons), the FR experiment exhibits a negative SSA bias at the AERONET sites. This suggests the local overestimation of the absorbing aerosol fraction in the column-integrated background at these specific locations. The DA experiment effectively corrects this negative bias, reducing the RMSE from 0.091 to 0.059. Furthermore, DA experiment significantly increases the fraction of data points with absolute errors below 0.05 (from 30.21% to 60.28%), demonstrating improved simulations of aerosol absorption properties. This improvement highlights the advantage of assimilating speciated aerosol observations. Traditional assimilation of total aerosol extinction primarily scales the total aerosol mass, which largely preserves the background aerosol composition ratio and thus struggles to correct such localized SSA biases. In contrast, assimilating CALIOP speciated extinctions adjusts the 3D distribution of individual components. Through this spatially varying correction, the DA experiment successfully optimizes the relative proportions of scattering and absorbing aerosols at the AERONET sites, thereby improving the simulated SSA. It should be noted that the modeled SSA in the DA experiment is slightly underestimated compared to AERONET. This is an expected behavior inherited from the assimilated observations, as the synergistic CALIOP-MODIS retrieval algorithm tends to slightly overestimate the BC fraction, leading to a lower SSA relative to AERONET (Kudo et al., 2023). As shown in Figure 11, by independently adjusting individual aerosol components based on CALIOP speciated observations, the DA experiment successfully reduces both SSA BIAS and RMSE at 33 out of 36 AERONET sites (91.67%), yielding mean improvement rates of 33.56% and 29.82%, respectively.

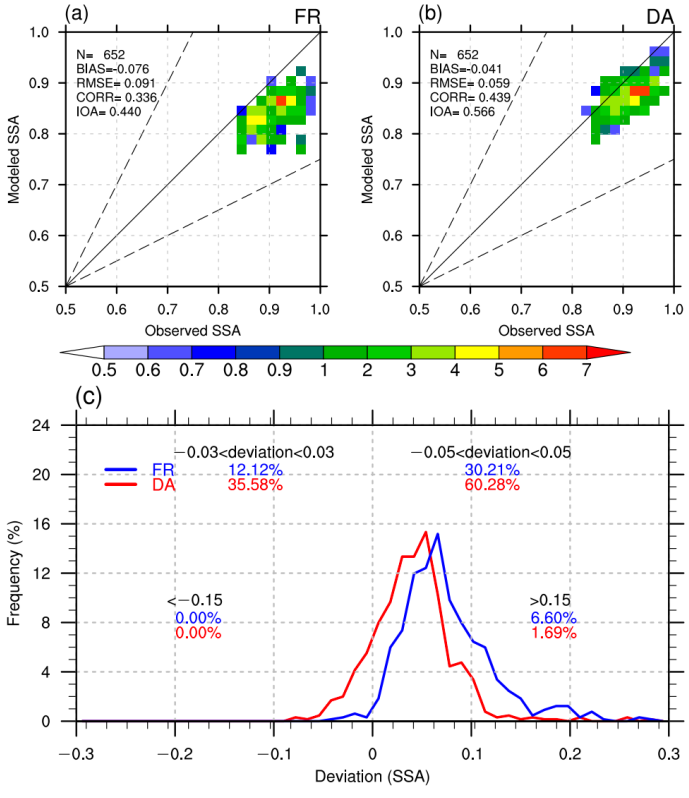

Figure 10. Same as Fig. 6 but for single scattering albedo (SSA).

https://doi.org/10.5194/egusphere-2026-2340
Preprint. Discussion started: 2 June 2026

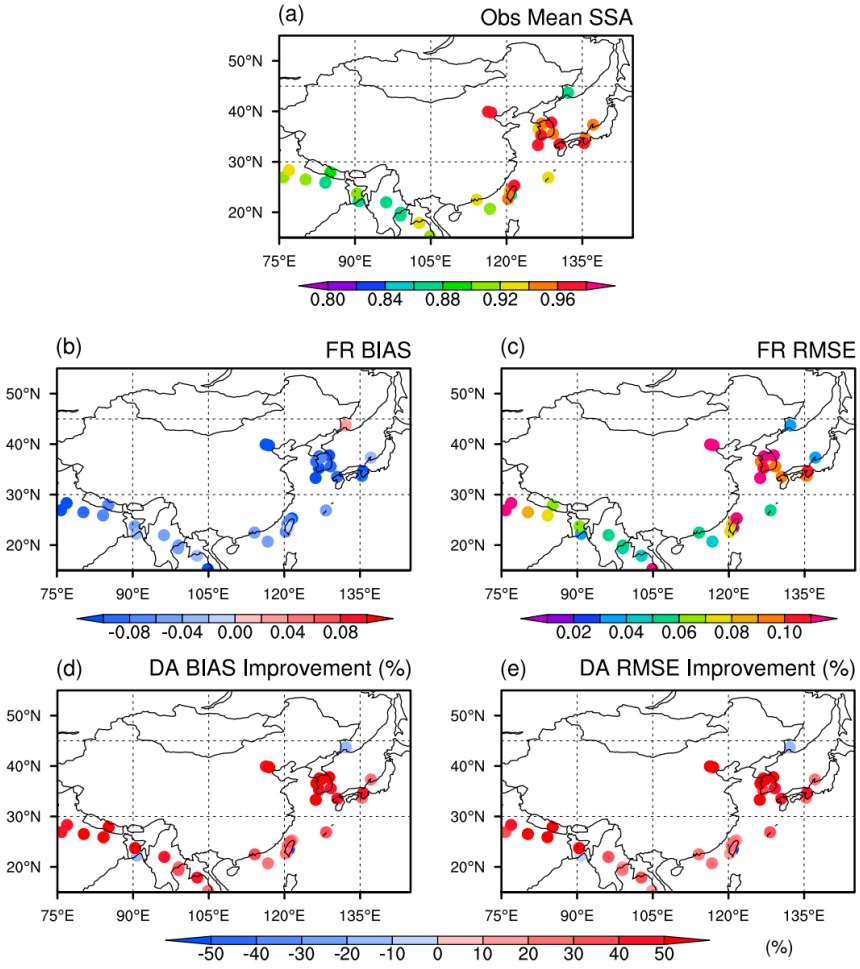

Figure 11. Same as Fig. 7 but for SSA.

Figure 12 presents the time series of simulated and observed SSA at four representative sites. At South Asian (Gandhi_College and Dhaka_University) and Southeast Asian (Mandalay_MTU) sites, the FR experiment consistently underestimates SSA. As shown in Figure 1, these regions are characterized by high loadings of BC and water-soluble aerosols, primarily driven by intense anthropogenic emissions and spring biomass burning. Although the domain-averaged background generally underestimates the BC fraction (as shown in Fig. 4), the persistent negative SSA bias at these specific locations indicates a local underestimation of the scattering-to-absorbing aerosol ratio. By assimilating CALIOP speciated observations, the DA experiment effectively constrains the concentrations of individual aerosol species, correcting this local imbalance. Consequently, DA significantly increases the simulated SSA, reducing the RMSE from 0.071 to 0.034 at Gandhi_College and from 0.060 to 0.037 at Mandalay_MTU. Similarly, at the downwind Fukuoka site in East Asia, aerosols are a complex mixture influenced by the long-range transport of dust and anthropogenic pollutants. The DA experiment also successfully corrects the underestimated SSA, reducing the RMSE from 0.100 to 0.052. These results demonstrate that the

https://doi.org/10.5194/egusphere-2026-2340
Preprint. Discussion started: 2 June 2026

speciated assimilation dynamically optimizes the aerosol composition, leading to a more accurate representation of aerosol optical properties across both source and downwind regions. It is worth noting that traditional assimilation of total AOT merely scales the total aerosol mass, which preserves the model's background aerosol composition ratio. Consequently, pure AOT assimilation struggles to correct structural biases in aerosol optical properties like SSA. In contrast, by explicitly assimilating component-specific extinction profiles, our DA system independently adjusts the mass of scattering and absorbing species, thereby successfully correcting the local scattering-to-absorbing ratio and significantly improving the simulated SSA.

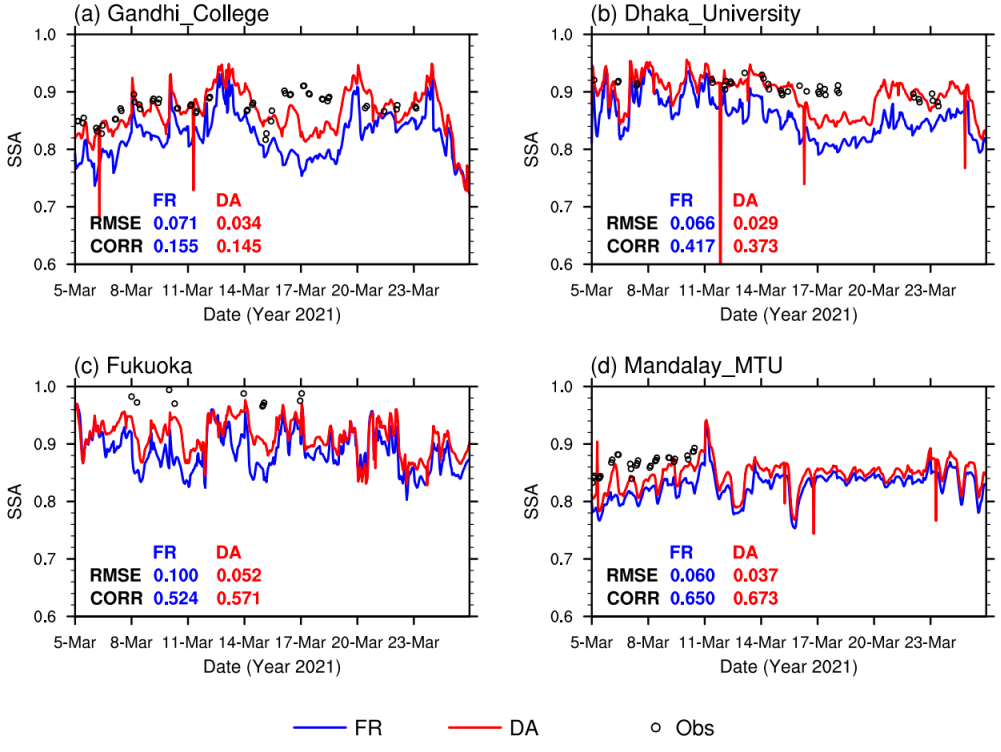

Figure 12. Same as Fig. 8 but for SSA.

4.4 Radiative heating response to optimized aerosol vertical profiles

Figure 13 illustrates the mean vertical profiles of the shortwave (SW) heating rate along the CALIOP tracks. To isolate the instantaneous radiative impact of the assimilated aerosols, the DA heating rates are diagnosed by updating the model restart files with the analysis aerosol fields and integrating the radiation scheme for a single time step. Compared to the FR experiment, the DA experiment produces a distinct warming effect in the lower to middle troposphere (2-6 km), with a maximum heating rate increase of approximately 3.0 K day^{-1} at 4-5 km. As indicated by the vertical aerosol distributions in Figure 4, this mid-level heating peak can be physically interpreted as the superposition of the elevated BC layer (peaking around 6 km) and the lower-level dust layer (peaking near 1 km). Since the shortwave heating rate is determined by both the

https://doi.org/10.5194/egusphere-2026-2340
Preprint. Discussion started: 2 June 2026

aerosol absorption capacity and the available downward solar radiation flux, the combination of these absorbing aerosols culminates in the strongest heating response at 4-5 km. This significant mid-level warming suggests that the assimilation effectively corrects the underestimation of absorbing aerosols in these layers. Figure 14 presents the relationship between the assimilation-induced increments in extinction coefficient and SW heating rate. The samples are categorized into three regimes based on their Single Scattering Albedo (SSA). The scatter plot and corresponding linear regressions reveal a clear, quantitative dependence of heating efficiency on aerosol absorption properties. For highly absorbing aerosols (SSA < 0.85), a small increment in extinction leads to a sharp increase in the SW heating rate, as indicated by the steepest slope. As the SSA increases to intermediate values (0.85 < SSA < 0.92), the slope decreases, reflecting a moderate heating response. For predominantly scattering aerosols (SSA > 0.92), the heating efficiency per unit extinction is the lowest among the three categories. This distinct stratification confirms that atmospheric SW heating is not only determined by total aerosol loading, but also fundamentally governed by the proportion of absorbing components (e.g., black carbon and dust) that directly convert intercepted solar radiation into thermal energy.

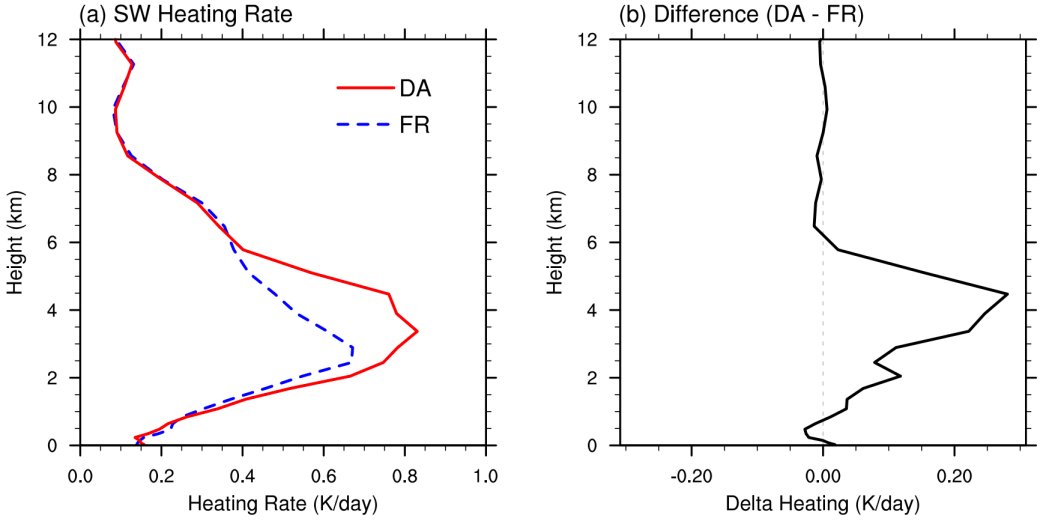

Figure 13. Vertical profiles of the shortwave (SW) heating rate. (a) Comparison of the mean SW heating rate (units: K day^{-1}) between the FR and DA experiment. (b) The vertical profile of the heating rate difference (DA minus FR). The profiles are averaged along the CALIOP track.

https://doi.org/10.5194/egusphere-2026-2340
Preprint. Discussion started: 2 June 2026

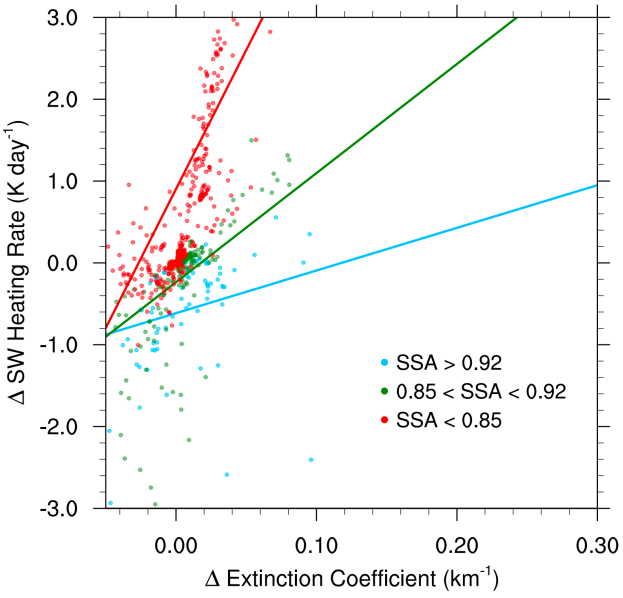

Figure 14. Response of shortwave radiative heating to aerosol extinction perturbations derived from data assimilation. The samples are categorized by SSA into three groups: SSA < 0.85 (red), 0.85 < SSA < 0.92 (green), and SSA > 0.92 (blue), the solid lines represent linear regressions for each category.

To investigate the physical mechanisms of aerosol radiative effects across different source regions, Figure 15 presents the latitude-height cross-sections of speciated aerosol extinction and the corresponding shortwave (SW) heating rates. The spatial distribution of aerosols exhibits strong latitudinal gradients due to varying regional emissions and transport patterns. Compared to CALIOP observations, the FR experiment fails to reproduce the vertical distribution of aerosol species, while the DA experiment effectively corrects these vertical structures. The differences between the DA and FR experiments (DA-FR) reveal a strong dependence of the SW heating rate on the distribution of black carbon (BC). For instance, north of 40°N, although the assimilation decreases the dust extinction, it significantly increases the BC concentration. Because BC is highly absorbing, its increase dominates the local radiative response, leading to a net positive SW heating anomaly in this region. Similarly, at lower latitudes (15°N–23°N), the DA experiment introduces a substantial increase in BC at elevated layers (2-6 km). The spatial pattern of the enhanced SW heating perfectly mirrors this BC increment, confirming that BC is the primary driver of the mid-level atmospheric warming. Conversely, a prominent negative SW heating anomaly (reduced heating) appears in the lower troposphere (below 2 km) at these lower latitudes (15°N–23°N). This cooling effect is driven by two mechanisms: first, the dense layer of absorbing BC aloft acts as a radiative shield, significantly attenuating the downward solar radiation that reaches the lower atmosphere; second, the simultaneous reduction of both BC and scattering water-soluble aerosols in the lower layers further diminishes local absorption. Ultimately, this vertical radiative heating structure, strong warming aloft and reduced heating below, can decrease the environmental temperature lapse rate and enhance the

https://doi.org/10.5194/egusphere-2026-2340
Preprint. Discussion started: 2 June 2026

static stability of the lower troposphere. This highlights the importance of accurately simulating the vertical distribution of individual aerosol species for radiative forcing assessments.

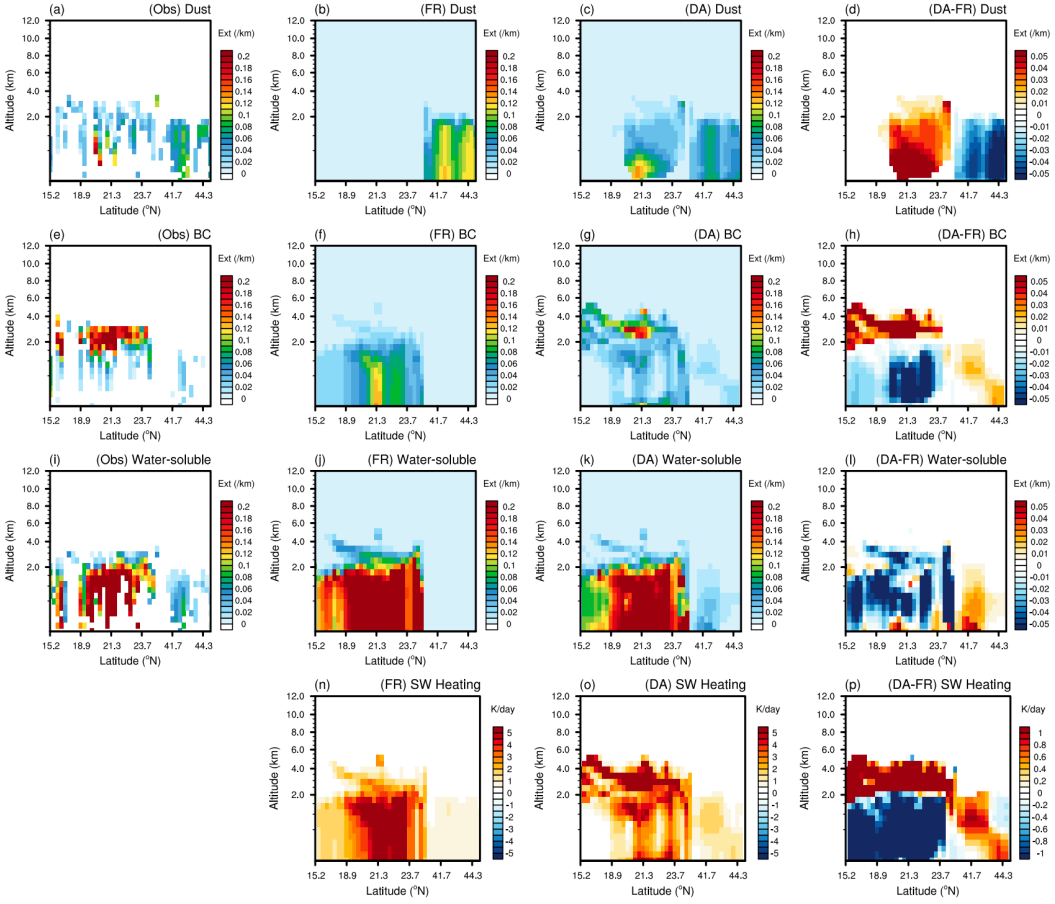

Figure 15. Latitude-height cross-sections of aerosol component extinctions and SW heating rates along the CALIOP track at 06:00 UTC March 7, 2021. (a-l) Comparison of extinction coefficients (units: km^{-1}) for Dust, BC, and Water-soluble species among CALIOP observations, FR, and DA experiments including the difference (DA minus FR). (n-p) Similar to upper panels but for the SW heating rate (units: K day^{-1}).

5. Conclusion and Discussion

Accurate quantification of aerosol direct radiative forcing (DRF) remains a significant challenge in climate modeling, largely due to persistent uncertainties in the vertical distribution of distinct aerosol components. Traditional data assimilation (DA) methods relying on column-integrated optical depth or bulk extinction often fail to constrain the specific aerosol composition, leading to misrepresentations of aerosol absorption and scattering properties. To address this under-constrained problem, we developed a component-resolved four-dimensional local ensemble transform Kalman filter (4D-LETKF) system with spatial and observational constraints within the WRF-Chem model. By assimilating CALIOP-MODIS synergistic retrievals of

https://doi.org/10.5194/egusphere-2026-2340
Preprint. Discussion started: 2 June 2026

species-specific extinction profiles, this system explicitly optimizes the three-dimensional mass distributions of individual aerosol components (dust, sea salt, black carbon, and water-soluble aerosols) over East Asia.

Our evaluations demonstrate that the component-resolved DA experiment substantially improves the spatiotemporal representation of complex aerosol mixtures. The free-running (FR) experiment exhibited systematic underestimations of aerosol loadings and completely missed elevated black carbon (BC) plumes. In contrast, the DA experiment successfully reconstructed the vertical structures of all four aerosol components. A major advancement of this system is its ability to capture persistent free-tropospheric BC layers over the Indian subcontinent. Such features are frequently missed by chemical transport models due to emission inventory deficiencies and have historically required sparse in-situ balloon or aircraft profiling to detect. Independent validations against ground-based AERONET and AD-Net lidar observations confirmed that the assimilation not only reduced the biases and root mean square errors (RMSEs) of column-integrated AOT, but also accurately captured the vertical evolution of long-range transport episodes. Furthermore, by independently adjusting the mass of scattering and absorbing species, the DA system effectively corrected local biases in the single scattering albedo (SSA), highlighting its unique capability to optimize fundamental aerosol optical properties. The optimized component-specific vertical profiles profoundly modulate the atmospheric shortwave (SW) radiative heating. Our results reveal that the heating efficiency is highly sensitive to the vertical partitioning of absorbing aerosols, particularly BC. The assimilation of elevated BC plumes induced a pronounced mid-tropospheric warming, accompanied by a reduction in lower-tropospheric heating due to the attenuation of downward solar radiation.

Furthermore, while the component-resolved assimilation system represents an advancement, several physical limitations should be acknowledged. First, the GOCART optical scheme treats aerosols as externally mixed spheres, whereas the assimilated CALIOP-MODIS retrieval assumes internal mixing. This discrepancy introduces representativeness errors in mass extinction efficiency and absorption. Recent studies demonstrate that particle size and mixing state strongly modulate single scattering albedo and radiative forcing, with biases up to -3.0 W m^{-2} in industrial regions (Tiwari et al., 2025; Guan et al., 2026a). Importantly, achieving accurate single scattering albedo requires more than mass adjustment alone, particle size and mixing state must also be accounted for (Tiwari et al., 2026), including changes in the spectral signature of absorption across wavebands (Guan et al., 2026b). Second, the elevated BC plumes captured in our analysis are not solely emission-driven, both orographic lofting and local buoyancy-induced factors impact transport from Southeast Asia into the free troposphere play critical roles (Cohen et al., 2017; Wang et al., 2021). Third, as demonstrated by Tiwari et al. (2025), jointly constraining BC mass and number can help distinguish between fresh emission hotspots and aging-dominated regions, while the additional datasets used in that study (TROPOMI UV, AERONET multi-wavelength SSA) are already available over East Asia and could be assimilated to further refine size and mixing-state estimates. Addressing these uncertainties will be essential for reducing biases in aerosol direct radiative forcing.

While this study emphasizes the critical role of component-resolved vertical structures in determining instantaneous radiative heating, the subsequent thermodynamic and dynamic feedbacks need further investigation. Future studies should explore how these component-driven heating rate anomalies perturb atmospheric temperature profiles and regional circulation fields.

https://doi.org/10.5194/egusphere-2026-2340
Preprint. Discussion started: 2 June 2026

In particular, the enhanced static stability induced by absorbing aerosols aloft can significantly suppress planetary boundary layer development. Investigating these aerosol-radiation-boundary layer interactions, and their two-way feedback mechanisms on the accumulation of surface pollutants and cloud formation, will be a crucial next step toward a more comprehensive understanding of aerosol-climate interactions. Additionally, future work will explore the assimilation of high-temporal-resolution aerosol component retrievals from ground-based networks, such as AD-Net and SKYNET, to further constrain the diurnal variations of aerosol vertical structures. Furthermore, recent advancements in passive remote sensing, such as the retrieval of black carbon using near-ultraviolet bands from GOSAT-2/CAI-2 imagers (Nakajima et al., 2026), provide unprecedented spatial coverage of absorbing aerosols. Assimilating these novel high-resolution passive retrievals over land areas, particularly over China and India, will be a highly promising direction to further constrain regional aerosol radiative forcing.

Code and data availability

The AERONET data can be accessed via https://aeronet.gsfc.nasa.gov/. The AD-Net lidar data are available at http://www-lidar.nies.go.jp/AD-Net. The CALIOP-MODIS synergistic aerosol component dataset can be obtained by contacting the National Institute for Environmental Studies (NIES) lidar team. The WRF-Chem model code is publicly available at https://www.mmm.ucar.edu/weather-research-and-forecasting-model.

Author contributions

YC and TD conceived the study and designed the component-resolved aerosol data assimilation framework. YC performed the control and assimilation experiments and conducted the data analysis. DG, KY, T. Nishizawa, MZ, RK, AH, YJ, AS, HP, GS, and T. Nakajima provided valuable comments on the paper. YC prepared the manuscript with contributions from TD and all other co-authors.

Acknowledgments

Model simulations were performed using EarthLab supercomputers at the Institute of Atmospheric Physics (IAP), China. We extend our thanks to the relevant researchers who provided AERONET observations. We are particularly grateful to the NIES lidar team for providing the ground-based lidar observations as well as the MODIS-CALIOP synergistic component aerosol product. Finally, we thank the anonymous reviewers for their valuable comments and constructive suggestions that helped improve this manuscript.

Financial support

This study was financially supported by the National Natural Science Foundation of China (grant no. 42305088), National Key Research and Development Program of China (grant no. 2024YFB3908701), the International Partnership Program of

Chinese Academy of Sciences (grant no. 060GJHZ2024090MI), the National Natural Science Foundation of China (grant nos. 42375190, 42405109), National Key Research and Development Program of China (grant no. 2025YFE0108100), Fundamental Research Funds of Institute of Atmospheric Physics, Chinese Academy of Sciences.

Competing interests

The contact author has declared that none of the authors has any competing interests.

References

Babu, S. S., Moorthy, K. K., Manchanda, R. K., Sinha, P. R., Satheesh, S. K., Vajja, D. P., Srinivasan, S., and Kumar, V. H. A.: Free tropospheric black carbon aerosol measurements using high altitude balloon: Do BC layers build "their own homes" up in the atmosphere?, Geophys. Res. Lett., 38, L08803, https://doi.org/10.1029/2011GL046654, 2011.

Benedetti, A., Morcrette, J.-J., Boucher, O., Dethof, A., Engelen, R. J., Fisher, M., Flentje, H., Huneeus, N., Jones, L., Kaiser, J. W., Kinne, S., Mangold, A., Razinger, M., Simmons, A. J., and Suttie, M.: Aerosol analysis and forecast in the European Centre for Medium-Range Weather Forecasts Integrated Forecast System: 2. Data assimilation, J. Geophys. Res., 114, D13205, https://doi.org/10.1029/2008JD011115, 2009.

Boylan, J. W. and Russell, A. G.: PM and light extinction model performance metrics, goals, and criteria for three-dimensional air quality models, Atmos. Environ., 40, 4946–4959, https://doi.org/10.1016/j.atmosenv.2005.09.087, 2006.

Campbell, J. R., Reid, J. S., Westphal, D. L., Zhang, J., Hyer, E. J., and Welton, E. J.: CALIOP Aerosol Subset Processing for Global Aerosol Transport Model Data Assimilation, IEEE J. Sel. Top. Appl. Earth Obs. Remote Sens., 3, 203–214, https://doi.org/10.1109/JSTARS.2010.2044868, 2010.

Chen, C., Dubovik, O., Schuster, G. L., Chin, M., Henze, D. K., Lapyonok, T., Li, Z., Derimian, Y., and Zhang, Y.: Multi-angular polarimetric remote sensing to pinpoint global aerosol absorption and direct radiative forcing, Nat. Commun., 13, 7459, https://doi.org/10.1038/s41467-022-35147-y, 2022.

Chen, D., Liu, Z., Ban, J., and Chen, M.: The 2015 and 2016 wintertime air pollution in China: SO2 emission changes derived from a WRF-Chem/EnKF coupled data assimilation system, Atmos. Chem. Phys., 19, 8619–8650, https://doi.org/10.5194/acp-19-8619-2019, 2019.

Chen, F., and Dudhia, J.: Coupling an advanced land surface-hydrology model with the Penn State-NCAR MM5 modeling system. Part I: Model implementation and sensitivity, Mon. Weather Rev., 129, 569–585, https://doi.org/10.1175/1520-0493(2001)129<0569:CAALSH>2.0.CO;2, 2001.

Cheng, X., Liu, Y., Xu, X., You, W., Zang, Z., Gao, L., Chen, Y., Su, D., and Yan, P.: Lidar data assimilation method based on CRTM and WRF-Chem models and its application in PM2.5 forecasts in Beijing, Sci. Total Environ., 682, 541–552, https://doi.org/10.1016/j.scitotenv.2019.05.186, 2019.

https://doi.org/10.5194/egusphere-2026-2340
Preprint. Discussion started: 2 June 2026

Chin, M., Ginoux, P., Kinne, S., Torres, O., Holben, B. N., Duncan, B. N., Martin, R. V., Logan, J. A., Higurashi, A., and Nakajima, T.: Tropospheric aerosol optical thickness from the GOCART model and comparisons with satellite and Sun photometer measurements, J. Atmos. Sci., 59, 461-483, https://doi.org/10.1175/1520-0469(2002)059<0461:TAOTFT>2.0.CO;2, 2002.

Cohen, J. B., Lecoeur, E., and Ng, D. H. L.: Decadal-scale relationship between measurements of aerosols, land-use change, and fire over Southeast Asia, Atmos. Chem. Phys., 17, 721–743, https://doi.org/10.5194/acp-17-721-2017, 2017.

Crippa, M., Guizzardi, D., Butler, T., Keating, T., Wu, R., Kaminski, J., Kuenen, J., Kurokawa, J., Chatani, S., Morikawa, T., Pouliot, G., Racine, J., Moran, M. D., Klimont, Z., Manseau, P. M., Mashayekhi, R., Henderson, B. H., Smith, S. J., Suchyta, H., Muntean, M., Solazzo, E., Banja, M., Schaaf, E., Pagani, F., Woo, J.-H., Kim, J., Monforti-Ferrario, F., Pisoni, E., Zhang, J., Niemi, D., Sassi, M., Ansari, T., and Foley, K.: The HTAP_v3 emission mosaic: Merging regional and global monthly emissions (2000–2018) to support air quality modelling and policies, Earth Syst. Sci. Data, 15, 2667–2694, https://doi.org/10.5194/essd-15-2667-2023, 2023.

Di Tomaso, E., Schutgens, N. A. J., Jorba, O., and Pérez García-Pando, C.: Assimilation of MODIS Dark Target and Deep Blue observations in the dust aerosol component of NMMB-MONARCH version 1.0, Geosci. Model Dev., 10, 1107–1129, https://doi.org/10.5194/gmd-10-1107-2017, 2017.

Dong, X., Wu, P., Wang, Y., Xi, B., and Huang, Y.: New Observational Constraints on Warm Rain Processes and Their Climate Implications, Geophys. Res. Lett., 48, https://doi.org/10.1029/2020GL091836, 2021.

Dubovik, O. and King, M. D.: A flexible inversion algorithm for retrieval of aerosol optical properties from Sun and sky radiance measurements, J. Geophys. Res., 105, 20673–20696, https://doi.org/10.1029/2000JD900282, 2000.

El Amraoui, L., Sič, B., Piacentini, A., Marécal, V., Frebourg, N., and Attié, J.-L.: Aerosol data assimilation in the MOCAGE chemical transport model during the TRAQA/ChArMEx campaign: lidar observations, Atmos. Meas. Tech., 13, 4645–4667, https://doi.org/10.5194/amt-13-4645-2020, 2020.

Escribano, J., Di Tomaso, E., Jorba, O., Klose, M., Ageitos, M. G., Macchia, F., Amiridis, V., Baars, H., Marinou, E., Proestakis, E., Urbanneck, C., Althausen, D., Bühl, J., Mamouri, R.-E., and Pérez García-Pando, C.: Assimilating spaceborne lidar dust extinction can improve dust forecasts, Atmos. Chem. Phys., 22, 535–560, https://doi.org/10.5194/acp-22-535-2022, 2022.

Fernald, F. G.: Analysis of atmospheric lidar observations: some comments, Appl. Opt., 23, 652–653, https://doi.org/10.1364/AO.23.000652, 1984.

Freitas, S. R., Longo, K. M., Chatfield, R., Latham, D., Silva Dias, M. A. F., Andreae, M. O., Prins, E., Santos, J. C., Gielow, R., and Carvalho Jr., J. A., and Artaxo, P.: Including the sub-grid scale plume rise of vegetation fires in low resolution atmospheric transport models, Atmos. Chem. Phys., 7, 3385–3398, https://doi.org/10.5194/acp-7-3385-2007, 2007.

Gao, L., Jiang, L., Sun, W., Yan, P., Qi, B., Ji, C., and Tao, F.: Data assimilation of ceilometer aerosol extinction coefficient profile contributes to predictions of the three-dimensional structures of aerosols in East China, J. Geophys. Res. Atmos., 130, e2024JD042408, https://doi.org/10.1029/2024JD042408, 2025.

https://doi.org/10.5194/egusphere-2026-2340
Preprint. Discussion started: 2 June 2026

Gaspari, G. and Cohn, S. E.: Construction of correlation functions in two and three dimensions, Q. J. Roy. Meteorol. Soc., 125, 723–757, https://doi.org/10.1002/qj.49712555417, 1999.

Giles, D. M., Sinyuk, A., Sorokin, M. G., Schafer, J. S., Smirnov, A., Slutsker, I., Eck, T. F., Holben, B. N., Lewis, J. R., Campbell, J. R., Welton, E. J., Korkin, S. V., and Lyapustin, A. I.: Advancements in the Aerosol Robotic Network (AERONET) Version 3 database – automated near-real-time quality control algorithm with improved cloud screening for Sun photometer aerosol optical depth (AOD) measurements, Atmos. Meas. Tech., 12, 169–209, https://doi.org/10.5194/amt-12-169-2019, 2019.

Grell, G. A. and Freitas, S. R.: A scale and aerosol aware stochastic convective parameterization for weather and air quality modeling, Atmos. Chem. Phys., 14, 5233–5250, https://doi.org/10.5194/acp-14-5233-2014, 2014.

Guan, L., Cohen, J. B., Wang, S., Tiwari, P., Liu, Z., Li, Z., and Qin, K.: In-tandem multi-waveband particulate absorption and size observations yield substantial changes in radiative forcing over industrial Central China, Atmos. Chem. Phys., 26, 3107–3123, https://doi.org/10.5194/acp-26-3107-2026, 2026a.

Guan, L., Cohen, J. B., Wang, S., Tiwari, P., Liu, Z., and Qin, K.: Improving aerosol absorption estimates via size-resolved constraints based on AERONET and in situ measurements, Geophys. Res. Lett., 53, e2025GL117418, https://doi.org/10.1029/2025GL117418, 2026b.

Haywood, J. M., and Ramaswamy, V.: Global sensitivity studies of the direct radiative forcing due to anthropogenic sulfate and black carbon aerosols, J. Geophys. Res. Atmos., 103, 6043–6058, https://doi.org/10.1029/97JD03426, 1998.

Hersbach, H., Bell, B., Berrisford, P., Hirahara, S., Horányi, A., Muñoz-Sabater, J., Nicolas, J., Peubey, C., Radu, R., Schepers, D., Simmons, A., Soci, C., Abdalla, S., Abellan, X., Balsamo, G., Bechtold, P., Biavati, G., Bidlot, J., Bonavita, M., De Chiara, G., Dahlgren, P., Dee, D., Diamantakis, M., Dragani, R., Flemming, J., Forbes, R., Fuentes, M., Geer, A., Haimberger, L., Healy, S., Hogan, R. J., Hólm, E., Janisková, M., Keeley, S., Laloyaux, P., Lopez, P., Lupu, C., Radnoti, G., de Rosnay, P., Rozum, I., Vamborg, F., Villaume, S., and Thépaut, J.-N.: The ERA5 global reanalysis, Q. J. Roy. Meteorol. Soc., 146, 1999–2049, https://doi.org/10.1002/qj.3803, 2020.

Holben, B. N., Eck, T. F., Slutsker, I., Tanré, D., Buis, J. P., Setzer, A., Vermote, E., Reagan, J. A., Kaufman, Y. J., Nakajima, T., Lavenu, F., Jankowiak, I., and Smirnov, A.: AERONET – A Federated Instrument Network and Data Archive for Aerosol Characterization, Remote Sens. Environ., 66, 1–16, https://doi.org/10.1016/S0034-4257(98)00031-5, 1998.

Hong, S.-Y., Noh, Y., and Dudhia, J.: A new vertical diffusion package with an explicit treatment of entrainment processes, Mon. Weather Rev., 134, 2318–2341, https://doi.org/10.1175/MWR3199.1, 2006.

Hu, X.-M., Nielsen-Gammon, J. W., and Zhang, F.: Evaluation of Three Planetary Boundary Layer Schemes in the WRF Model, J. Appl. Meteorol. Clim., 49, 1831–1844, https://doi.org/10.1175/2010JAMC2432.1, 2010.

Huang, B., Pagowski, M., Trahan, S., Martin, C. R., Tangborn, A., Kondragunta, S., and Kleist, D. T.: JEDI-Based Three-Dimensional Ensemble-Variational Data Assimilation System for Global Aerosol Forecasting at NCEP, J. Adv. Model. Earth Syst., 15, e2022MS003232, https://doi.org/10.1029/2022MS003232, 2023.

https://doi.org/10.5194/egusphere-2026-2340
Preprint. Discussion started: 2 June 2026

Iacono, M. J., Delamere, J. S., Mlawer, E. J., Shephard, M. W., Clough, S. A., and Collins, W. D.: Radiative forcing by long-lived greenhouse gases: Calculations with the AER radiative transfer models, J. Geophys. Res., 113, D13103, https://doi.org/10.1029/2008JD009944, 2008.

IPCC: Climate Change 2021: The Physical Science Basis. Contribution of Working Group I to the Sixth Assessment Report of the Intergovernmental Panel on Climate Change, edited by: Masson-Delmotte, V., Zhai, P., Pirani, A., Connors, S. L., Péan, C., Berger, S., Caud, N., Chen, Y., Goldfarb, L., Gomis, M. I., Huang, M., Leitzell, K., Lonnoy, E., Matthews, J. B. R., Maycock, T. K., Waterfield, T., Yelekçi, O., Yu, R., and Zhou, B., Cambridge University Press, Cambridge, UK and New York, NY, USA, https://doi.org/10.1017/9781009157896, 2021.

Jin, J., Pang, M., Segers, A., Han, W., Fang, L., Li, B., Feng, H., Lin, H. X., and Liao, H.: Inverse modeling of the 2021 spring super dust storms in East Asia, Atmos. Chem. Phys., 22, 6393–6410, https://doi.org/10.5194/acp-22-6393-2022, 2022.

Koffi, B., Schulz, M., Bréon, F.-M., Dentener, F., Steensen, B. M., Griesfeller, J., Winker, D., Balkanski, Y., Bauer, S. E., Bellouin, N., Berntsen, T., Bian, H., Chin, M., Diehl, T., Easter, R., Ghan, S., Hauglustaine, D. A., Iversen, T., Kirkevåg, A., Liu, X., Lohmann, U., Myhre, G., Rasch, P., Seland, Ø., Skeie, R. B., Steenrod, S. D., Stier, P., Tackett, J., Takemura, T., Tsigaridis, K., Vuolo, M. R., Yoon, J., and Zhang, K.: Evaluation of the aerosol vertical distribution in global aerosol models through comparison against CALIOP measurements: AeroCom phase II results, J. Geophys. Res. Atmos., 121, 7254–7283, https://doi.org/10.1002/2015JD024639, 2016.

Kudo, R., Higurashi, A., Oikawa, E., Fujikawa, M., Ishimoto, H., and Nishizawa, T.: Global 3-D distribution of aerosol composition by synergistic use of CALIOP and MODIS observations, Atmos. Meas. Tech., 16, 3835–3863, https://doi.org/10.5194/amt-16-3835-2023, 2023.

Li, J., Carlson, B. E., Yung, Y. L., Lv, D., Hansen, J., Penner, J. E., Liao, H., Ramaswamy, V., Kahn, R. A., Zhang, P., Dubovik, O., Ding, A., Lacis, A. A., Zhang, L., and Dong, Y.: Scattering and absorbing aerosols in the climate system, Nat. Rev. Earth Environ., 3, 363–379, https://doi.org/10.1038/s43017-022-00296-7, 2022.

Li, Z. Q., Xu, H., Li, K. T., Li, D. H., Xie, Y. S., Li, L., Zhang, Y., Gu, X. F., Zhao, W., Tian, Q. J., Deng, R. R., Su, X. L., Huang, B., Qiao, Y. L., Cui, W. Y., Hu, Y., Gong, C. L., Wang, Y. Q., Wang, X. F., Wang, J. P., Du, W. B., Pan, Z. Q., Li, Z. Z., and Bu, D.: Comprehensive Study of Optical, Physical, Chemical, and Radiative Properties of Total Columnar Atmospheric Aerosols over China: An Overview of Sun–Sky Radiometer Observation Network (SONET) Measurements, Bull. Am. Meteorol. Soc., 99, 739–755, https://doi.org/10.1175/BAMS-D-17-0133.1, 2018.

Liu, Y., Lin, T., Hong, J., Wang, Y., Shi, L., Huang, Y., Wu, X., Zhou, H., Zhang, J., and de Leeuw, G.: Multi-dimensional satellite observations of aerosol properties and aerosol types over three major urban clusters in eastern China, Atmos. Chem. Phys., 21, 12331–12358, https://doi.org/10.5194/acp-21-12331-2021, 2021.

Lu, C.-H., Liu, Q., Wei, S.-W., Johnson, B. T., Dang, C., Stegmann, P. G., Grogan, D., Ge, G., Hu, M., and Lueken, M.: The Aerosol Module in the Community Radiative Transfer Model (v2.2 and v2.3): accounting for aerosol transmittance effects on the radiance observation operator, Geosci. Model Dev., 15, 1317–1329, https://doi.org/10.5194/gmd-15-1317-2022, 2022.

https://doi.org/10.5194/egusphere-2026-2340
Preprint. Discussion started: 2 June 2026

Mishra, A. K., Koren, I., and Rudich, Y.: Effect of aerosol vertical distribution on aerosol-radiation interaction: A theoretical prospect, Heliyon, 1, e00036, https://doi.org/10.1016/j.heliyon.2015.e00036, 2015.

Miyoshi, T., Yamane, S., and Enomoto, T.: Localizing the Error Covariance by Physical Distances within a Local Ensemble Transform Kalman Filter (LETKF), SOLA, 3, 89–92, https://doi.org/10.2151/sola.2007-023, 2007.

Nakajima, T., Sekiguchi, M., Momoi, M., Shi, C., Hashimoto, M., Babu, S. S., Gogoi, M. M., Goto, D., Madhavan, B. L., Nakajima, T. Y., Shiomi, K., Takenaka, H., Tang, C., Yao, R., Imasu, R., and Matsunaga, T.: Aerosol retrievals from the GOSAT-2/CAI-2 imager with the 2nd version of the multi-wavelength and multi-pixel method, J. Quant. Spectrosc. Radiat. Transf., 109939, https://doi.org/10.1016/j.jqsrt.2026.109939, 2026.

Nishizawa, T., Okamoto, H., Sugimoto, N., Matsui, I., Shimizu, A., and Aoki, K.: An algorithm that retrieves aerosol properties from dual-wavelength polarized lidar measurements, J. Geophys. Res., 112, D06212, https://doi.org/10.1029/2006JD007435, 2007.

Noh, Y. M., Lee, K., Kim, K., Shin, S.-K., Müller, D., and Shin, D. H.: Influence of the vertical absorption profile of mixed Asian dust plumes on aerosol direct radiative forcing over East Asia, Atmos. Environ., 138, 191–204, https://doi.org/10.1016/j.atmosenv.2016.04.044, 2016.

Oikawa, E., Nakajima, T., and Winker, D.: An Evaluation of the Shortwave Direct Aerosol Radiative Forcing Using CALIOP and MODIS Observations, J. Geophys. Res. Atmos., 123, 1211–1233, https://doi.org/10.1002/2017JD027247, 2018.

Pang, M., Jin, J., Yang, T., Chen, X., Segers, A., Buyantogtokh, B., Gu, Y., Li, J., Lin, H. X., Liao, H., and Han, W.: The sensitivity of aerosol data assimilation to vertical profiles: case study of dust storm assimilation with LOTOS-EUROS v2.2, Geosci. Model Dev., 18, 3781–3798, https://doi.org/10.5194/gmd-18-3781-2025, 2025.

Peng, Z., Lei, L., Liu, Z., Sun, J., Ding, A., Ban, J., Chen, D., Kou, X., and Chu, K.: The impact of multi-species surface chemical observation assimilation on air quality forecasts in China, Atmos. Chem. Phys., 18, 17387–17404, https://doi.org/10.5194/acp-18-17387-2018, 2018.

Proestakis, E., Amiridis, V., Marinou, E., Binietoglou, I., Ansmann, A., Wandinger, U., Hofer, J., Yorks, J., Nowottnick, E., Makhmudov, A., Papayannis, A., Pietruczuk, A., Gialitaki, A., Apituley, A., Szkop, A., Muñoz Porcar, C., Bortoli, D., Dionisi, D., Althausen, D., Mamali, D., Balis, D., Nicolae, D., Tetoni, E., Liberti, G. L., Baars, H., Mattis, I., Stachlewska, I. S., Voudouri, K. A., Mona, L., Mylonaki, M., Perrone, M. R., Costa, M. J., Sicard, M., Papagiannopoulos, N., Siomos, N., Burlizzi, P., Pauly, R., Engelmann, R., Abdullaev, S., and Pappalardo, G.: EARLINET evaluation of the CATS Level 2 aerosol backscatter coefficient product, Atmos. Chem. Phys., 19, 11743–11764, https://doi.org/10.5194/acp-19-11743-2019, 2019.

Rubin, J. I., Reid, J. S., Hansen, J. A., Anderson, J. L., Holben, B. N., Xian, P., Westphal, D. L., and Zhang, J.: Assimilation of AERONET and MODIS AOT observations using variational and ensemble data assimilation methods and its impact on aerosol forecasting skill, J. Geophys. Res. Atmos., 122, 4967–4992, https://doi.org/10.1002/2016JD026067, 2017.

https://doi.org/10.5194/egusphere-2026-2340
Preprint. Discussion started: 2 June 2026

Samset, B. H., and Myhre, G.: Vertical dependence of black carbon, sulphate and biomass burning aerosol radiative forcing: Vertical Dependence of Aerosol Forcing, Geophys. Res. Lett., 38, https://doi.org/10.1029/2011GL049697, 2011.

Samset, B. H., Myhre, G., Schulz, M., Balkanski, Y., Bauer, S., Berntsen, T. K., Bian, H., Bellouin, N., Diehl, T., Easter, R. C., Ghan, S. J., Iversen, T., Kinne, S., Kirkevåg, A., Lamarque, J.-F., Lin, G., Liu, X., Penner, J. E., Seland, Ø., Skeie, R. B., Stier, P., Takemura, T., Tsigaridis, K., and Zhang, K.: Black carbon vertical profiles strongly affect its radiative forcing uncertainty, Atmos. Chem. Phys., 13, 2423–2434, https://doi.org/10.5194/acp-13-2423-2013, 2013.

Schutgens, N., Tsyro, S., Gryspeerdt, E., Goto, D., Weigum, N., Schulz, M., and Stier, P.: On the spatio-temporal representativeness of observations, Atmos. Chem. Phys., 17, 9761–9780, https://doi.org/10.5194/acp-17-9761-2017, 2017.

Sekiyama, T. T., Tanaka, T. Y., Shimizu, A., and Miyoshi, T.: Data assimilation of CALIPSO aerosol observations, Atmos. Chem. Phys., 10, 39–49, https://doi.org/10.5194/acp-10-39-2010, 2010.

Shimizu, A., Sugimoto, N., Matsui, I., Arao, K., Uno, I., Murayama, T., Kagawa, N., Aoki, K., Uchiyama, A., and Yamazaki, A.: Continuous observations of Asian dust and other aerosols by polarization lidars in China and Japan during ACE-Asia, J. Geophys. Res., 109, D19S17, https://doi.org/10.1029/2002JD003253, 2004.

Sinyuk, A., Holben, B. N., Eck, T. F., Giles, D. M., Slutsker, I., Korkin, S., Schafer, J. S., Smirnov, A., Sorokin, M., and Lyapustin, A.: The AERONET Version 3 aerosol retrieval algorithm, associated uncertainties and comparisons to Version 2, Atmos. Meas. Tech., 13, 3375–3411, https://doi.org/10.5194/amt-13-3375-2020, 2020.

Sugimoto, N., Uno, I., Nishikawa, M., Shimizu, A., Matsui, I., Dong, X., Chen, Y., and Quan, H.: Record heavy Asian dust in Beijing in 2002: Observations and model analysis of recent events, Geophys. Res. Lett., 30, 1640, https://doi.org/10.1029/2002GL016349, 2003.

Sunilkumar, K., Ajay, A., Anand, N., Dharmesh, T., Stalin, P. G., Kapardhi, B. V. N., Santosh, K., Moorthy, K. K., and Satheesh, S. K.: Persistent Elevated Black Carbon Aerosol Layers in the Upper Troposphere and Its Linkage to Aircraft Emissions, Geophys. Res. Lett., 52, e2024GL113363, https://doi.org/10.1029/2024GL113363, 2025.

Thompson, G., Field, P. R., Rasmussen, R. M., and Hall, W. D.: Explicit forecasts of winter precipitation using an improved bulk microphysics scheme. Part II: Implementation of a new snow parameterization, Mon. Weather Rev., 136, 5095–5115, https://doi.org/10.1175/2008MWR2387.1, 2008.

Tiwari, P., Cohen, J. B., Lu, L., Wang, S., Li, X., Guan, L., Liu, Z., Li, Z., and Qin, K.: Multi-platform observations and constraints reveal overlooked urban sources of black carbon in Xuzhou and Dhaka, Commun. Earth Environ., 6, 38, https://doi.org/10.1038/s43247-025-02012-x, 2025.

Tiwari, P., Cohen, J. B., Gao, H., Lu, L., Wang, J., Dubovik, O., and Qin, K.: Microphysical evolution and column loading drive nonlinear regional contrast in black carbon top-of-atmosphere forcing, EGUsphere [preprint], https://doi.org/10.5194/egusphere-2026-363, 2026.

Tsikerdekis, A., Schutgens, N. A. J., and Hasekamp, O. P.: Assimilating aerosol optical properties related to size and absorption from POLDER/PARASOL with an ensemble data assimilation system, Atmos. Chem. Phys., 21, 2637–2674, https://doi.org/10.5194/acp-21-2637-2021, 2021.

https://doi.org/10.5194/egusphere-2026-2340
Preprint. Discussion started: 2 June 2026

Wang, S., Cohen, J. B., Deng, W., Qin, K., and Guo, J.: Using a new top-down constrained emissions inventory to attribute the previously unknown source of extreme aerosol loadings observed annually in the Monsoon Asia free troposphere, Earth's Future, 9, e2021EF002167, https://doi.org/10.1029/2021EF002167, 2021.

Wang, D., You, W., Zang, Z., Pan, X., Hu, Y., and Liang, Y.: A three-dimensional variational data assimilation system for aerosol optical properties based on WRF-Chem v4.0: design, development, and application of assimilating Himawari-8 aerosol observations, Geosci. Model Dev., 15, 1821–1840, https://doi.org/10.5194/gmd-15-1821-2022, 2022.

Welton, E. J., Voss, K. J., Quinn, P. K., Flatau, P. J., Markowicz, K., Campbell, J. R., Spinhirne, J. D., Gordon, H. R., and Johnson, J. E.: Measurements of aerosol vertical profiles and optical properties during INDOEX 1999 using micropulse lidars, J. Geophys. Res., 107, 8019, https://doi.org/10.1029/2000JD000038, 2002.

Wiedinmyer, C., Kimura, Y., McDonald-Buller, E. C., Emmons, L. K., Buchholz, R. R., Tang, W., Seto, K., Joseph, M. B., Barsanti, K. C., Carlton, A. G., and Yokelson, R.: The Fire INventory from NCAR version 2.5: an updated global fire emissions model for climate and chemistry applications, Geosci. Model Dev., 16, 3873–3915, https://doi.org/10.5194/gmd-16-3873-2023, 2023.

Willmott, C. J., Robeson, S. M., and Matsuura, K.: A refined index of model performance, Int. J. Climatol., 32, 2088–2094, https://doi.org/10.1002/joc.2419, 2012.

Yang, T., Li, H., Wang, H., Sun, Y., Chen, X., Wang, F., Xu, L., and Wang, Z.: Vertical aerosol data assimilation technology and application based on satellite and ground lidar: A review and outlook, J. Environ. Sci., 123, 292–305, https://doi.org/10.1016/j.jes.2022.04.012, 2023.

Ye, H., Pan, X., You, W., Zhu, X., Zang, Z., Wang, D., Zhang, X., Hu, Y., and Jin, S.: Impact of CALIPSO profile data assimilation on 3-D aerosol improvement in a size-resolved aerosol model, Atmos. Res., 264, 105877, https://doi.org/10.1016/j.atmosres.2021.105877, 2021.

Yumimoto, K., Tanaka, T. Y., Oshima, N., and Maki, T.: JRAero: the Japanese Reanalysis for Aerosol v1.0, Geosci. Model Dev., 10, 3225–3253, https://doi.org/10.5194/gmd-10-3225-2017, 2017.

Yumimoto, K., Tanaka, T. Y., Yoshida, M., Kikuchi, M., Nagao, T. M., Murakami, H., and Maki, T.: Assimilation and Forecasting Experiment for Heavy Siberian Wildfire Smoke in May 2016 with Himawari-8 Aerosol Optical Thickness, J. Meteorol. Soc. Jpn. Ser. II, 96B, 133–149, https://doi.org/10.2151/jmsj.2018-035, 2018.

Zeng, Y., Wang, M., Zhao, C., Chen, S., Liu, Z., Huang, X., and Gao, Y.: WRF-Chem v3.9 simulations of the East Asian dust storm in May 2017: modeling sensitivities to dust emission and dry deposition schemes, Geosci. Model Dev., 13, 2125–2147, https://doi.org/10.5194/gmd-13-2125-2020, 2020.

Zhang, J., Campbell, J. R., Reid, J. S., Westphal, D. L., Baker, N. L., Campbell, W. F., and Hyer, E. J.: Evaluating the impact of assimilating CALIOP-derived aerosol extinction profiles on a global mass transport model, Geophys. Res. Lett., 38, https://doi.org/10.1029/2011GL047737, 2011.

https://doi.org/10.5194/egusphere-2026-2340
Preprint. Discussion started: 2 June 2026

Zhang, L., Li, J., Jiang, Z., Dong, Y., Ying, T., and Zhang, Z.: Clear-Sky Direct Aerosol Radiative Forcing Uncertainty Associated with Aerosol Vertical Distribution Based on CMIP6 models, J. Clim., 35, 3021–3035, https://doi.org/10.1175/JCLI-D-21-0479.1, 2022.